

Scalable Bayesian Clustering for Integrative Analysis of Multi-View Data

Rafael Cabral¹, Maria de Iorio^{1,2}, Andrew Harris¹

¹Department of Paediatrics, Yong Loo Lin School of Medicine, National University of Singapore

²Singapore Institute for Clinical Sciences, A*STAR

September 2, 2024

Abstract

In the era of Big Data, scalable and accurate clustering algorithms for high-dimensional data are essential. We present new Bayesian Distance Clustering (BDC) models and inference algorithms with improved scalability while maintaining the predictive accuracy of modern Bayesian non-parametric models. Unlike traditional methods, BDC models the distance between observations rather than the observations directly, offering a compromise between the scalability of distance-based methods and the enhanced predictive power and probabilistic interpretation of model-based methods. However, existing BDC models still rely on performing inference on the partition model to group observations into clusters. The support of this partition model grows exponentially with the dataset's size, complicating posterior space exploration and leading to many costly likelihood evaluations. Inspired by K-medoids, we propose using tessellations in discrete space to simplify inference by focusing the learning task on finding the best tessellation centers, or “medoids.” Additionally, we extend our models to effectively handle multi-view data, such as data comprised of clusters that evolve across time, enhancing their applicability to complex datasets. The real data application in numismatics demonstrates the efficacy of our approach.

Keywords: Bayesian non-parametrics, Bayesian Distance Clustering, Voronoi Tessellation, K-medoids, Scalability

1 Introduction

There is a need for scalable Bayesian clustering algorithms that allow for uncertainty in the number of clusters K . Traditional probabilistic Bayesian models with posterior inference, like mixture models (Mclachlan and Basford, 1988; Fraley and Raftery, 2002) and species sampling

processes (Pitman, 1996) (e.g., the Dirichlet process), are often slow and not scalable. On the other hand, distance-based clustering tools in the machine learning community, like K-means and K-medoids, though fast, do not provide uncertainty quantification and tend to perform poorly in complex scenarios (Hastie et al., 2009). A middle ground is thus desirable.

Duan and Dunson (2021), Rigon et al. (2023), and Natarajan et al. (2023) introduce a new class of Bayesian Distance Clustering (BDC) models to address the previous issues. Let $\mathcal{T} = \{\mathcal{C}_1, \dots, \mathcal{C}_K\}$ denote the partition of N objects into K clusters, where \mathcal{C}_k is a set containing the indexes of the objects in cluster k . BDC consists in eliciting a likelihood on the distance matrix $\mathbf{D} = [d(x_i, x_j)]_{ij}$ for some distance metric d instead of eliciting a likelihood on the data $\mathbf{x} = \{x_1, \dots, x_N\}$ directly. For a review, see Xu and Tian (2015). By not modeling the data directly, we achieve greater robustness with regard to model assumptions. Natarajan et al. (2023) specify a likelihood for pairwise distances as follows

$$\pi(\mathbf{D} \mid \boldsymbol{\theta}, \boldsymbol{\lambda}, \mathcal{T}) = \underbrace{\prod_{k=1}^N \prod_{\substack{i, j \in \mathcal{C}_k \\ i < j}} f(D_{ij} \mid \lambda_k)}_{\text{cohesion}} \underbrace{\prod_{(k, t) \in A} \prod_{\substack{i \in \mathcal{C}_k \\ j \in \mathcal{C}_t}} g(D_{ij} \mid \theta_{kt})}_{\text{repulsion}} \quad (1)$$

where $A = \{(k, t) : 1 \leq k < t \leq K\}$, and f and g are probability densities. The likelihood incorporates cohesion and repulsion terms to ensure clusters are composed of objects with small internal dissimilarities (cohesion) and clear separation from other clusters (repulsion). The repulsion term also enhances cluster identifiability. This approach addresses the lack of probabilistic interpretation in distance-based clustering methods and the lack of computational scalability in traditional probabilistic Bayesian models. See Natarajan et al. (2023) and Rigon et al. (2023) for a theoretical justification.

A crucial aspect of BDC is eliciting an adequate prior on the partition \mathcal{T} . Popular choices in the Bayesian non-parametric literature involve prior on partitions implied by a species sampling model (Pitman, 1996) where the probability of $\mathcal{T} = \{\mathcal{C}_1, \dots, \mathcal{C}_K\}$ is given by $p(n_1, \dots, n_K)$, where $n_k = |\mathcal{C}_k|$ denotes the number of elements in \mathcal{C}_k . The function p is a symmetric function of its arguments and is known as the exchangeable partition probability function (EPPF).

However, the previous models for the partition \mathcal{T} have a large support which grows according to the Bell number of N , making posterior exploration through MCMC difficult and leading to inference algorithms that are not scalable. This paper builds upon the BDC model

in Natarajan et al. (2023) and introduces new partition models for BDC with the accompanying inference algorithms. We take inspiration from K-Medoids (Kaufman and Rousseeuw, 2009) and infer probabilistically which observations are the “medoids” instead of performing inference on the random partition model \mathcal{T} directly. In more detail, each medoid is associated with a cluster, and then the clusters are defined by assigning the objects that are closest to the respective medoid in terms of some distance. As will be explained in Section 2.2, this amounts to performing a Voronoi tessellation in discrete space. This procedure improves computational efficiency since inference on the medoids is often easier and more scalable. It also permits the specification of likelihoods on the distance matrix that can be evaluated with linear computational complexity instead of quadratic complexity. Our simulations show that the new models yield comparable, sometimes better, predictive performance while significantly reducing computational time compared to the BDC models of Natarajan et al. (2023), while also allowing for uncertainty quantification on K , the number of clusters. On the other hand, the predictive performance is considerably higher than that of K-medoid implementations, especially in scenarios where the data is noisy, and there is overlap in the cluster groups. We discuss the relationship with K-medoids by showing that the K-medoid estimate can be seen as a maximum a posteriori estimate of the class of BDC models with the tessellation priors we propose.

The second main contribution is introducing BDC models for multi-view data to cluster objects that contain several features, where there is a possibly distinct partition for each feature (see Duan (2020), Franzolini et al. (2023) and references therein). For instance, consider data whose clustering changes at different measurement times. In this case, each measurement time corresponds to a different feature. These data are frequently found in applications, and we extend our previous BDC construction to model the distance matrices of all features jointly, accounting for dependencies between the partition of each feature.

This paper is structured as follows. In Section 2, we cover the basics of BDC and introduce partitions models defined through tessellations in discrete space. Next, in Section 3, we present BDC for multi-view data. Section 4 presents the main simulation results, Section 5 applies the methodology to a problem from digital numismatics, and finally, in Section 6, we discuss the main results and present directions for future work.

2 Bayesian distance clustering with tessellation priors

For convenience, let us consider the cluster allocation labels z_i where $z_i = j$ if $i \in \mathcal{C}_j$ and let $[N] = \{1, \dots, N\}$ denote the index set of all N objects.

2.1 Likelihood specification

The first term of the likelihood in (1) should favor clusters composed of objects with small dissimilarities among themselves (cohesion), while the second term should favor large dissimilarities to objects in other clusters (repulsion). To achieve the previous cohesion behavior, we set f in (1) to be the density function of a $\text{Gamma}(\delta_1, \lambda_k)$ distribution, with $\delta_1 < 1$, so that the density is decreasing and thus penalizing large distances among objects in the same cluster. Conversely, to achieve the repulsion behavior, we set g in (1) to be the density function of a $\text{Gamma}(\delta_2, \theta_{kt})$, with $\delta_2 > 1$ so that the $g(0|\theta_{kt}) = 0$ and increasing near 0 in order to penalize small distances among objects in different clusters. Further, for computational convenience, we elicit conjugate priors,

$$\lambda_k \stackrel{i.i.d.}{\sim} \text{Gamma}(\mu, \beta) \quad \theta_{kt} \stackrel{i.i.d.}{\sim} \text{Gamma}(\zeta, \gamma)$$

where λ_k is a rate parameter of f specific for each cluster and θ_{kt} is the rate parameter of g specific for each pair of clusters. These parameters control the dispersion in the pairwise distances of objects in the same cluster and objects in different pairs of clusters, respectively.

To set the hyperparameters $\delta_1, \delta_2, \mu, \beta, \zeta$, and γ , we follow the empirical Bayes procedure laid out in Algorithm 1 of Natarajan et al. (2023). Finally, we can integrate out λ_k and θ_{kt} from $\pi(\mathbf{D} | \boldsymbol{\theta}, \boldsymbol{\lambda}, \mathcal{T})$ and calculate a closed-form expression for the marginal likelihood $\pi(\mathbf{D} | \mathcal{T})$ conditionally only on the partition \mathcal{T} . Performing inference directly on $\pi(\mathbf{D} | \mathcal{T})$ will speed up computations by avoiding estimating λ_k and θ_{kt} . The density $\pi(\mathbf{D} | \mathcal{T})$ is derived in Appendix A.

The model is completed by specifying a prior on the partition \mathcal{T} . A common choice is the EPPF of the Dirichlet process Ferguson (1973). We will compare the new partition models introduced in the next section with the EPPF derived from the Pitman-Yor process (PY). For further information, see Pitman (1995). The EPPF of the PY process is

$$\pi(n_1, \dots, n_K) = \frac{[M + \theta]_{K-1; \theta}}{[M + 1]_{N-1; 1}} \prod_{i=1}^K [1 - \varphi]_{n_i-1; 1} \quad (2)$$

where for real numbers x and a and non-negative integer m

$$[x]_{m;a} = \begin{cases} 1 & \text{for } m = 0, \\ x(x+a) \dots (x+(m-1)a) & \text{for } m = 1, 2, \dots \end{cases}$$

In (2), K denotes the number of clusters in \mathcal{T} , $M > 0$ is a concentration parameter, and $0 \leq \varphi < 1$ is a discount parameter. When $\varphi = 0$, the Pitman-Yor process simplifies to the Dirichlet process. Performing inference in BDC with the previous partition priors or the exchangeable sequence of cluster partition prior utilized in Natarajan et al. (2023) can lead to issues in terms of scalability and poor mixing and convergence for high-dimensional data. To overcome these challenges, we introduce next a prior on the partition defined through an extension of Voronoi tessellations to discrete space. This approach is adopted in a different context in Boom et al. (2023) to cluster nodes on a graph.

2.2 Voronoi tessellation models in discrete space

Voronoi tessellations as defined in Denison et al. (2002) split a continuous space \mathcal{X} into K regions, with tessellation centers t_1, \dots, t_K . Points are assigned to a region R_i based on their “distance” from the centers, so that $R_i = \{x \in \mathcal{X} : d(x, t_i) < d(x, t_j) \text{ for all } j \neq i\}$, where d is a predefined distance metric defined for all points $x_1, x_2 \in \mathcal{X}$. See Figure 1 for a visual illustration where d is the Euclidean distance.

We extend the previous definition of Voronoi tessellation to discrete space. Unlike tessellations in continuous space, where any point in \mathcal{X} could be a tessellation center, we assume that the tessellation centers must correspond to one of the N objects, thus easing the search for the optimal tessellation centers. The remaining objects are assigned to clusters based on the pairwise distances with the tessellation centers. We also refer to the tessellation centers t_i as “medoids” to highlight similarities with the standard K-Medoids clustering. Let γ be the set containing the K indexes of the medoids. For example, if $\gamma = \{5, 10, 20\}$ then the objects with indexes 5, 10 and 20 are the medoids. Similarly to Voronoi tessellations in continuous space, we assign all the objects nearest to medoid i to cluster i :

$$\mathcal{C}_i(\mathbf{D}, \gamma) = \{j \in [N] : \arg \min_{l \in \gamma} D_{lj} = i\} \quad \text{which define the partition model} \quad (3)$$

$$\mathcal{T}(\mathbf{D}, \gamma) = \{\mathcal{C}_1(\mathbf{D}, \gamma), \mathcal{C}_2(\mathbf{D}, \gamma), \dots, \mathcal{C}_K(\mathbf{D}, \gamma)\}$$

We emphasize that the partition \mathcal{T} is a deterministic function of both the medoid set γ and the distance matrix \mathbf{D} , $\mathcal{T}(\mathbf{D}, \gamma)$, but to simplify notation, we will often refer to it as \mathcal{T} . We also assume that the minimization in (3) has always a unique solution.

Since the partition \mathcal{T} is deterministic given γ and \mathbf{D} , we elicit the likelihood in Section 2.1 conditionally on the medoid set γ . By abusing notation, we consider $\pi(\mathbf{D}|\gamma) = \pi(\mathbf{D}|\mathcal{T}(\mathbf{D}, \gamma))$. We then elicit a prior distribution on γ and perform inference on γ by approximating the posterior density

$$\pi(\gamma|\mathbf{D}) = \frac{\pi(\mathbf{D}|\gamma)\pi(\gamma)}{\int \pi(\mathbf{D}|\gamma)\pi(\gamma)d\gamma} \quad (4)$$

Lastly, when computing posterior samples of γ , we also automatically obtain posterior samples of the partition $\mathcal{T}(\mathbf{D}, \gamma)$ which informs about the clustering structure of the data.

Performing inference on the medoid set γ instead of the partition model \mathcal{T} leads to several computational advantages. First, the sample space being explored is much smaller: given N objects, there are $2^N - 1$ different allowed sets for γ since each object can either be a medoid or not, and we exclude the case where no object is a medoid. On the other hand, in typical random partition models, the number of possible partitions for a set of size N is the Bell number B_N , which grows much faster than $2^N - 1$. Secondly, there are efficient and easy-to-implement algorithms to perform inference on these models. In this paper, we implement a birth-death algorithm, where at each step of the Metropolis-Hastings algorithm, we generate a new γ proposals by adding or removing a medoids in the medoids set, followed by a move step where a medoid is changed at random keeping K fixed. It is also possible to consider a Gibbs sampler, and these algorithms are detailed in the Appendix D.1.

Lastly, this formulation also allows for alternative likelihood specifications, which are more computationally efficient to evaluate. To improve scalability, we modify the cohesion term of (1), and instead of modeling all pairwise distances between objects in the same cluster, we only model the distances between the objects in a cluster and the cluster medoid. Likewise, for the repulsion term, we only model the distances between the medoids, instead of all pairwise distances between objects in different clusters. The new likelihood is

$$\pi^{\text{lin}}(\mathbf{D} | \gamma, \boldsymbol{\lambda}) = \underbrace{\prod_{i \in \gamma} \prod_{j \in \mathcal{C}_i(\mathbf{D}, \gamma) \setminus \{i\}} f(D_{ij} | \lambda_i)}_{\text{cohesion}} \underbrace{\prod_{\substack{i, j \in \gamma \\ i \neq j}} g(D_{ij})}_{\text{repulsion}} \quad (5)$$

The computational complexity of evaluating the previous likelihood is linear in N (hence the

superscript “lin” for linear), unlike (1), which is quadratic. Similarly to (1), we can also integrate out $\boldsymbol{\lambda}$, and express the likelihood conditionally only on $\boldsymbol{\gamma}$ (and the hyperparameters $\delta_1, \delta_2, \mu, \beta$ and θ). The likelihood is given by

$$\pi(\mathbf{D} \mid \boldsymbol{\gamma}) = \prod_{i=1}^K \mathcal{L}_k^{(1)} \prod_{0 < i < j < K} \mathcal{L}_{ij}^{(2)}, \quad \text{where}$$

$$\mathcal{L}_i^{(1)} = \frac{\Gamma(\delta_1)^{-n_k^*} \Gamma(\mu + n_k^* \delta_1)}{\Gamma(\mu)} \beta^\mu \left(\prod_{j \in \mathcal{C}_i(\mathbf{D}, \boldsymbol{\gamma}) \setminus \{i\}} D_{ij} \right)^{\delta_1 - 1} \left(\beta + \sum_{j \in \mathcal{C}_i(\mathbf{D}, \boldsymbol{\gamma}) \setminus \{i\}} D_{ij} \right)^{-\mu - \delta_1 n_k^*}$$

$$\mathcal{L}_{ij}^{(2)} = \text{Gamma}(D_{ij}; \delta_2, \theta)$$

where $n_k^* = |\mathcal{C}_k| - 1$, and $\text{Gamma}(D_{ij}; \delta_2, \theta)$ is the density function of a Gamma distribution with shape parameter δ_2 and rate parameter θ . Appendix B describes a procedure in the spirit of empirical Bayes, similar to the one in Natarajan et al. (2023), to select the hyperparameters $\delta_1, \delta_2, \mu, \beta$, and θ .

2.3 Prior on the medoid set

We consider prior distributions on $\boldsymbol{\gamma}$ that only reflect prior beliefs on the number of clusters K , i.e. given K , the prior on the possible centers is uniform. These priors take the form $\pi(\boldsymbol{\gamma}, K) = \binom{N}{K}^{-1} \pi(K)$, $0 < K = |\boldsymbol{\gamma}| \leq N$, where $\pi(K)$ is the prior distribution on the number of clusters. In our context, it is natural to elicit a prior that penalizes the number of clusters, such as

$$\pi(\boldsymbol{\gamma}) = \binom{N}{K}^{-1} \times \text{TGeom}(K; p) \quad 0 < K = |\boldsymbol{\gamma}| \leq N \quad (6)$$

where $\text{TGeom}(\cdot; p)$ is the probability mass function of a truncated geometric distribution with parameter p and support between 1 and N , inclusive. The first term ensures that any choice of K medoids from N objects is equally likely, and the second term penalizes the number of medoids since it decreases with K .

2.4 Computational complexity and properties

Table 1 outlines the worst-case computational complexity of performing a likelihood evaluation based on (1) and (5) and considering K fixed. Additionally, we consider the scenario where

only the cohesion term is present. In Big Data applications, a computational complexity of $\mathcal{O}(N^2)$ can be prohibitive, especially since such likelihood evaluations must be performed thousands or even millions of times during MCMC inference. In these cases, distance-based clustering based on (5) is more desirable due to its linear computational complexity (assuming $K \ll N$ when considering the repulsion term).

	Cohesion	Cohesion + Repulsion
‘Quadratic’ Likelihood in (1)	$\mathcal{O}(N^2)$	$\mathcal{O}(N^2)$
‘Linear’ Likelihood in (5)	$\mathcal{O}(N)$	$\mathcal{O}(N + K^2)$

Table 1: Computational complexity of the likelihood evaluations in (1) and (5), with and without the repulsion term.

In the birth-death algorithm (Appendix D.1), besides performing a likelihood evaluation at each MCMC iteration, we also need to find the tessellation configuration given a set of centers as in (3), and so the computational complexity of each MCMC iteration is $\mathcal{O}(NK + L)$, where L is the computational complexity of one likelihood evaluation given in Table 1. In the Gibbs sampler MCMC algorithm, we cycle through each object, and for each object, we perform two tessellations and two likelihood evaluations, so the computational complexity per iteration is $\mathcal{O}(N(NK + L))$. On the other hand, the computational complexity of the K-medoids algorithm PAM (Partitioning Around Medoids) is $\mathcal{O}(N(N - K)^2)$. More scalable K-medoid algorithms are available, including CLARA (Clustering Large Applications) and CLARANS (Clustering Large Applications based upon RANdomized Search) (Schubert and Rousseeuw, 2019). Even though K-medoid algorithms are faster, they perform considerably worse when the data is noisy, and the clusters overlap, as shown in Section 4.

The tessellation $\mathcal{T}(\gamma, \mathbf{D})$ depends on the choice of a specific distance metric to compute \mathbf{D} . Here, we investigate the properties of the tessellation, such as exchangeability, microclustering, and projectivity. The microclustering property means that $M_N/N \rightarrow 0$ in probability, where M_N is the size of the largest cluster, and is a relevant property in several applications (Miller et al., 2015). Proposition 1 shows that this property is not present for an arbitrary matrix \mathbf{D} . A sequence of random partitions $\{\mathcal{T}_N\}_{N=1}^\infty$ is projective (or Kolmogorov consistent) if \mathcal{T}_N is equal in distribution to the restriction of \mathcal{T}_M to $[N]$ for $1 \leq N < M$. This property, however, is not appropriate for medoid-based clustering since the prior on the medoid set depends on

N (the support is $1, 2, \dots, N$).

Proposition 1. Exchangeability: Let σ be a finite permutation of the indexes $1, 2, \dots, N$, let \mathcal{T}^* be the partition \mathcal{T} after the permutation, and let $\mathbf{D}^* = [D_{\sigma(i),j}]_{i,j}$ be the distance matrix after permuting the rows. Then, for (1) and (5), $\pi(\mathbf{D}^*|\mathcal{T}^*) = \pi(\mathbf{D}|\mathcal{T})$. *Microclustering:* Consider an arbitrary distance matrix \mathbf{D} and prior $\pi(\gamma)$. The induced prior on the partition given in (3), $\mathcal{T}(\gamma, \mathbf{D})$, does not satisfy the microclustering property.

Proof. The proof is given in Appendix D.2. □

2.5 Relationship with K-medoids

Traditional K-medoid clustering algorithms also aim at identifying which objects should be the “medoids.” For a review see Kaufman and Rousseeuw (2009) and Jain (2010). Formally, the K-medoid estimate for γ is the solution of the following optimization problem:

$$\hat{\gamma} = \arg \min_{\gamma} \sum_{i \in \gamma} \sum_{j \in \mathcal{C}_i(\mathbf{D}, \gamma) \setminus \{i\}} D_{ij} \quad (7)$$

We assign all the non-medoid objects nearest to medoid i to cluster i , also according to (3), and the optimization consists of searching for the set of K medoids that minimize the distance between each medoid i and the non-medoid objects assigned to cluster i . The K-medoids estimate is the maximum a posteriori estimate of the BDC model in (5) for specific choices of f , g and prior $\pi(\gamma)$. More in detail, let us consider the the density $f(D_{ij}|\lambda_i) \propto \exp(-D_{ij})$, ignore the repulsion term, and consider the prior $\pi(\gamma) \propto I[|\gamma| = K]$ so that the number of medoids is fixed to K . Then, the K-medoids estimate is the mode of the posterior density

$$\pi(\gamma | \mathbf{D}) \propto \exp \left(- \sum_{i \in \gamma} \sum_{j \in \mathcal{C}_i(\mathbf{D}, \gamma) \setminus \{i\}} D_{ij} \right) I[|\gamma| = K]$$

where the ensuing partition estimate is given by $\hat{\mathcal{T}}(\mathbf{D}, \hat{\gamma}) = \{\mathcal{C}_1(\mathbf{D}, \hat{\gamma}), \dots, \mathcal{C}_K(\mathbf{D}, \hat{\gamma})\}$. The advantage of our Bayesian formulation is the ability to quantify uncertainty on the partition and number of clusters. Also, as shown in the simulations, our MCMC algorithms are more robust in locating the modal region in a variety of scenarios compared to the standard algorithms utilized in K-medoids.

As an additional point, Rigon et al. (2023) demonstrate that the K-means estimate is also a maximum a posteriori estimate of a Bayesian model with posterior density $\pi(\mathcal{T}|\mathbf{x}) \propto$

$\exp\left(-\sum_{i=1}^K \sum_{k \in \mathcal{C}_i} \|x_i - \tilde{x}_k\|_2^2\right) I[|\mathcal{T}| = K]$, where $\tilde{x}_k = (1/|\mathcal{C}_k|) \sum_{i \in \mathcal{C}_k} x_i$ represents the centroid of cluster k . The resulting partition can be seen as a Voronoi tessellation in continuous space where the objects of cluster \mathcal{C}_k belong to the region R_k in Section 2.2 with center $t_k = \tilde{x}_k$. On the other hand, our partitions are defined through the medoids as in (3), and require performing Voronoi tessellation in discrete space. Rigon et al. (2023) also introduce the concept of a partition “medoid,” defined for cluster k as $\arg \min_{i \in \mathcal{C}_k} \tilde{D}(x_i, X_k)$, where $\tilde{D}(x_i, X_k)$ denotes the overall distance between object i and the other objects in cluster k . However, the authors did not establish the link between their Bayesian models and K-medoids. They do not use the medoid set to define the partition model, as described in (3). Instead, they utilize partition models to define the medoids. Consequently, their approach involves performing inference on the partition model rather than directly on the medoid set, resulting in less computationally efficient algorithms.

3 Bayesian distance clustering for multi-view data

Datasets frequently present multivariate information often collected across distinct domains and with different feature support spaces. For instance, in our numismatics application, we have information about each coin’s obverses and reverses. Another example is in longitudinal data analysis, where the underlying clustering structure of individuals is likely to change over time. Data of this type are often referred to as multi-view data, and the number and shapes of clusters may need to vary across features to accurately capture dependence structures and heterogeneity. For a review of clustering models for multi-view data, see Franzolini et al. (2023). However, existing models for clustering multi-view data are based on modeling the data directly rather than the distance matrix, and here, we examine the latter. We consider N objects with M features, and so there are M distance matrices $\mathbf{D}^{(i)}$ for $i = 1, \dots, M$ with dimensions $N \times N$ pertaining to each feature.

Previous work, such as Caron et al. (2017), De Iorio et al. (2019), and Page et al. (2022), focus on modeling dependencies between random partition models. Since we model the medoid set directly and not the partition, the models in the previous papers cannot be applied directly. This section discusses two approaches to model dependencies between partitions in BDC with partitions defined through tessellations. One model assumes an order among features, i.e.,

a particular feature is considered as a reference, while the second model is more flexible. Following the notation in Franzolini et al. (2023), we refer to different features as “layers.” The partition of layer i is given by $\mathcal{T}_i = \{\mathcal{C}_{i,1}, \dots, \mathcal{C}_{i,K_i}\}$ where $\mathcal{C}_{i,j}$ is the cluster j of layer i which is defined similarly to (3) by grouping together the objects that are closest to medoid j according to the distance matrix $\mathbf{D}^{(i)}$. Without loss of generality, we focus on the case where the N objects have only two layers. We thus define two medoid sets γ_1 and γ_2 that induce two partitions \mathcal{T}_1 and \mathcal{T}_2 to cluster the first and second layers, respectively. Similarly to Page et al. (2022), the joint likelihood of the distance matrices of the first and second layers, $\mathbf{D}^{(1)}$ and $\mathbf{D}^{(2)}$, are conditionally independent given the previous medoid sets. The posterior distribution is

$$\begin{aligned} \pi(\gamma_1, \gamma_2 \mid \mathbf{D}^{(1)}, \mathbf{D}^{(2)}) &\propto \pi(\mathbf{D}^{(1)} \mid \mathcal{T}_1) \pi(\mathbf{D}^{(2)} \mid \mathcal{T}_2) \pi(\gamma_1, \gamma_2) \\ \mathcal{T}_1 &= \mathcal{T}_1(\gamma_1, \mathbf{D}^{(1)}), \quad \mathcal{T}_2 = \mathcal{T}_2(\gamma_2, \mathbf{D}^{(2)}, \cdot) \end{aligned} \quad (8)$$

where \mathcal{T}_2 can additionally depend on γ_1 and $\mathbf{D}^{(1)}$. This section presents two priors for $\pi(\gamma_1, \gamma_2)$ that account for dependencies in the medoids sets and, thus, on the ensuing partitions. Lastly, we consider a dependent random partition model $\pi(\mathcal{T}_1, \mathcal{T}_2)$ where the marginal distributions $\pi(\mathcal{T}_1)$ and $\pi(\mathcal{T}_2)$ are given by the EPPF in (2).

3.1 Tessellation models for nested partitions

Let us consider the cluster allocation labels $\mathbf{z}_i = \{z_{i1}, \dots, z_{iN}\}$ that specify the clusters of each object at layer i , where if $z_{ij} = k$ then object j belongs to the k th cluster of layer i ($j \in \mathcal{C}_{i,k}$). Let us also consider $\gamma_i = \{\gamma_{i1}, \dots, \gamma_{iK_i}\}$, which contain the indexes of the K_i medoids at layer i (the order of this indexes is arbitrary).

Definition 3.1. In a nested partition model for two layers, two objects belong to the same cluster at layer two only if they belong to the same cluster at layer one. Formally,

$$z_{2i} = z_{2j} \implies z_{1i} = z_{1j}, \quad \forall i, j \in [N]$$

where the reverse implication is not assumed.

The previous definition leads to partitions where the number of clusters in the second layer is always larger than in the first layer, and the clusters of the second layer are “inside” the clusters of the first layer (see Figure 1 for a representation in continuous space).

We now consider a natural extension of the Voronoi tessellation models of Section 2.2 that lead to nested partitions. For the cluster allocation labels of the first layer, we proceed as in Section 2.2. The label of object j corresponds to the index of the closest medoid:

$$z_{1j}(\boldsymbol{\gamma}_1, \mathbf{D}^{(1)}) = \arg \min_{i \in [K_1]} D_{\boldsymbol{\gamma}_1^{(i)}, j}^{(1)} \quad (9)$$

For instance, take $\boldsymbol{\gamma}_1 = \{2, 5\}$ (2 medoids) and the first row of the distance matrix $\mathbf{D}_{1,\cdot}^{(1)} = [0, 3, 1, 10, 4]$. Then, the first object is closest to the medoid object with index 2 (first medoid), so $z_{11} = 1$. We proceed similarly for layer 2, but instead of searching for the minimum distance between object j and all of the medoids of the second layer $\boldsymbol{\gamma}_2$, the optimization considers only the medoids in $\boldsymbol{\gamma}_2$ also belonging to $\mathcal{C}_{1,z_{1,j}}$, the cluster at layer one that object j belong to:

$$z_{2j}(\boldsymbol{\gamma}_2, \mathbf{D}^{(2)}, \mathcal{T}_1) = \arg \min_{l \in \boldsymbol{\gamma}_2 \cap \mathcal{C}_{1,z_{1,j}}} D_{lj}^{(2)} \quad (10)$$

The only restriction on the medoids sets $\boldsymbol{\gamma}_1$ and $\boldsymbol{\gamma}_2$ is that $\boldsymbol{\gamma}_2 \cap \mathcal{C}_{1,z_{1,j}}$ should not be an empty set, and so at least one object in $\mathcal{C}_{1,k}$ should be a medoid in the second layer. Figure 2.2 shows an example of a nested partition structure resulting from the tessellation of medoids $\boldsymbol{\gamma}_1$ and $\boldsymbol{\gamma}_2$ in continuous space. For the first layer, objects in regions A and B belong to the same cluster as the medoid located at (1.5, 2.5). In the second layer, region A is linked to the medoid at (0.5, 2.5), while region B is linked to the medoid at (2, 1.5).

The final model is given by (8), where (9) and (10) define the partition models $\mathcal{T}_1 = \mathcal{T}_1(\boldsymbol{\gamma}_1, \mathbf{D}^{(1)})$ and $\mathcal{T}_2 = \mathcal{T}_2(\boldsymbol{\gamma}_2, \mathbf{D}^{(2)}, \mathcal{T}_1)$ and we consider independent priors for $\boldsymbol{\gamma}_1$ and $\boldsymbol{\gamma}_2$ following equation (6). Appendix D.2 discusses extending the MCMC algorithm of the tessellation models of Section 2.2 to perform inference on these models.

3.2 Joint tessellation models

The previous nested tessellation model is restrictive in that the first-layer partition structure restricts the cluster allocations in the second layer. Two objects cannot belong to the same cluster in the second layer unless they also belong to the same cluster in the first layer. Consequently, the number of clusters in the second layer is always larger than in the first. Thus, we consider now more flexible dependent tessellation models.

Intuitively, we aim to include a dependence parameter $\alpha \in [0, 1]$ in our model, so that when $\alpha = 0$, $\boldsymbol{\gamma}_1$ is independent of $\boldsymbol{\gamma}_2$, and as α increases, the partitions \mathcal{T}_1 and \mathcal{T}_2 become

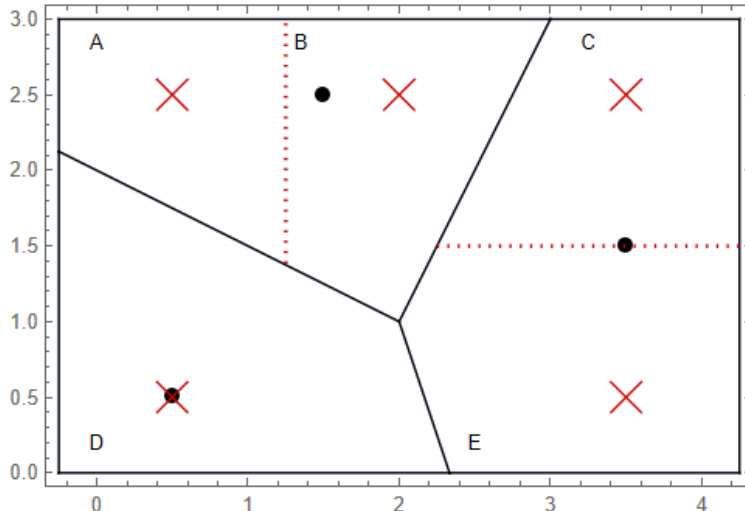


Figure 1: Example of a nested partition structure. The black lines delimit the three regions of the first layer. Both the black lines and red dotted lines delimit the five regions of the second layer. The black dots represent the medoids in the first layer, while the red crosses represent the medoids of the second layer.

increasingly similar. The joint prior can be expressed as $\pi(\gamma_1, \gamma_2 | \alpha) = \pi(\gamma_2 | \gamma_1, \alpha) \pi(\gamma_1)$, where $\pi(\gamma_2 | \gamma_1, \alpha)$ penalizes the “distance” between the induced partitions \mathcal{T}_1 and \mathcal{T}_2 .

Previous work, such as that by Dahl et al. (2023), introduces the concept of shrinking a random partition toward a reference partition. Paganin et al. (2021) multiply the partition prior $\pi(\mathcal{T}_1)$ by a penalization term leading to the conditional density $\pi(\mathcal{T}_2 | \mathcal{T}_1, \phi) \propto \pi(\mathcal{T}_1) \exp(-\phi d(\mathcal{T}_1, \mathcal{T}_2))$, where d quantifies the distance between partitions. However, these models apply to partitions and not medoid sets. Also, in the case of the random partitions in Paganin et al. (2021), the normalization constant of $\pi(\mathcal{T}_2 | \mathcal{T}_1, \phi)$ which is a function \mathcal{T}_1 and ϕ , is intractable, leading to the necessity of fixing parameters or relying on computationally expensive MCMC algorithms for doubly intractable problems.

To model the medoid set directly and maintain scalability while penalizing the distance between induced partitions, we adopt a generalized Bayes perspective (Bissiri et al., 2016; Miller, 2021). Bissiri et al. (2016) provide a coherent framework for general Bayesian inference where the parameters of interest are related to observations via a loss function instead of the traditional likelihood function, which can be too restrictive. For multi-view data, we start by

defining the loss function

$$l(\boldsymbol{\gamma}_1, \boldsymbol{\gamma}_2, \alpha) = -\log \pi(\mathbf{D}^{(1)}|\boldsymbol{\gamma}_1) - \log \pi(\mathbf{D}^{(2)}|\boldsymbol{\gamma}_2) + \phi(\alpha)d(\boldsymbol{\gamma}_1, \boldsymbol{\gamma}_2; \mathbf{D}^{(1)}, \mathbf{D}^{(2)})$$

where the distance measure is given by

$$d(\boldsymbol{\gamma}_1, \boldsymbol{\gamma}_2; \mathbf{D}^{(1)}, \mathbf{D}^{(2)}) = \frac{1}{\text{RI}(\mathcal{T}_1(\boldsymbol{\gamma}_1; \mathbf{D}^{(1)}), \mathcal{T}_2(\boldsymbol{\gamma}_2; \mathbf{D}^{(2)}))} - 1$$

Here, RI stands for the Rand Index. When $\mathcal{T}_1 = \mathcal{T}_2$, the RI is 1, resulting in a distance of 0. Conversely, if the partitions do not agree on any object, then RI is 0, and the distance becomes infinite. We employ the transformation $\phi(\alpha) = \alpha/(1 - \alpha)$ to ensure that $\alpha \in [0, 1]$. When $\alpha \rightarrow 0$, no penalty is induced, whereas larger values of α lead to larger penalization. A valid and coherent update for the model parameters is

$$\begin{aligned} \tilde{\pi}(\boldsymbol{\gamma}_1, \boldsymbol{\gamma}_2, \alpha|\mathbf{D}^{(1)}, \mathbf{D}^{(2)}) &= \frac{\exp(-l(\boldsymbol{\gamma}_1, \boldsymbol{\gamma}_2, \alpha))\pi(\boldsymbol{\gamma}_1, \boldsymbol{\gamma}_2, \alpha)}{\int \exp(-l(\boldsymbol{\gamma}_1, \boldsymbol{\gamma}_2, \alpha))\pi(\boldsymbol{\gamma}_1, \boldsymbol{\gamma}_2, \alpha)d\boldsymbol{\gamma}_1d\boldsymbol{\gamma}_2d\alpha} \\ &\propto \pi(\mathbf{D}^{(1)}|\boldsymbol{\gamma}_1)\pi(\mathbf{D}^{(2)}|\boldsymbol{\gamma}_2) \exp(-\phi(\alpha)d(\boldsymbol{\gamma}_1, \boldsymbol{\gamma}_2; \mathbf{D}^{(1)}, \mathbf{D}^{(2)}))\pi(\boldsymbol{\gamma}_1)\pi(\boldsymbol{\gamma}_2)\pi(\alpha) \end{aligned} \quad (11)$$

where the tilde in $\tilde{\pi}$ is meant to distinguish the previous posterior density from the more traditional ones based on a likelihood specification. Appendix D.3 provides the MCMC algorithm to perform inference, where we show that for the prior $\alpha \sim \text{Beta}(a, b)$ we can marginalize out α and model $\tilde{\pi}(\boldsymbol{\gamma}_1, \boldsymbol{\gamma}_2|\mathbf{D}^{(1)}, \mathbf{D}^{(2)})$ directly.

3.3 Stationary dependent random partitions models with EPPFs

We will compare the previous Bayesian tessellation models with known dependent random partition models in the Bayesian non-parametric literature. We emphasize that these models directly perform inference on the partition instead of the medoid set. In Page et al. (2022), \mathcal{T}_1 and \mathcal{T}_2 are made dependent by considering the auxiliary variables $\boldsymbol{\kappa} = \{\kappa_1, \dots, \kappa_n\}$ and the following relationship $\pi(\mathcal{T}_1, \mathcal{T}_2|\boldsymbol{\kappa}) = \pi(\mathcal{T}_2|\mathcal{T}_1, \boldsymbol{\kappa})\pi(\mathcal{T}_1)$, where $\pi(\mathcal{T}_1)$ is an EPPF. If $\kappa_i = 1$ then $z_{1i} = z_{2i}$, i.e., object i is assigned to the same cluster in both layers, while if $\kappa_i = 0$ then object i is subject to reallocation at layer 2 (it may still end in the same cluster as in layer 1). The prior $\kappa_i \stackrel{i.i.d.}{\sim} \text{Bernulli}(\alpha)$ is assigned, where if $\alpha = 0$, then \mathcal{T}_1 is independent from \mathcal{T}_2 and if $\alpha = 1$ then $\mathcal{T}_1 = \mathcal{T}_2$ with probability 1.

The previous construction leads to stationarity, in the sense that the marginal distribution of \mathcal{T}_2 is the same as \mathcal{T}_1 and is thus described by the same EPPF. We chose the Pitman-

Yor EPPF in (2) and employed a Gibbs sampler to perform inference, which is discussed in Appendix D.4.

4 Simulation study

The goal of the simulations is to compare the Bayesian models based on the tessellation of Sections 2.2, 3.1, and 3.2 with Bayesian non-parametric PY models and K-medoid algorithms. First, we describe the models and then the simulated data.

We consider the four likelihood configurations in Table 1, and for the PY models, we can only consider the “quadratic” (there are no medoids). We fit a joint model with likelihood given by (8) and consider a direct or induced prior on the partitions given next:

1. **PY independent:** Independent Pitman-Yor (PY) EPPF prior on each partition, employing a Gibbs sampler.
2. **PY joint:** Stationary and dependent prior for the two partitions with a PY marginal, as described in Section 3.3.
3. **Tessellation independent:** Partitions induced by independent tessellation for each layer, with the MCMC algorithm described in Algorithm 2.
4. **Tessellation nested:** Nested partitions induced by Bayesian tessellation models, as described in Section 3.1 and Algorithm 3.
5. **Tessellation joint:** Dependent partitions induced by joint tessellation models, as described in Section 3.2 and Algorithm 4.

Finally, we also compare the previous models with the standard K-medoid algorithms. We run the K-medoid algorithms available in the R package *cluster* (Maechler et al., 2019), fixing the number of clusters to the true value determined by a numismatic expert.

The MCMC algorithms for the previous models are described in Appendix D. For the PY partition models, we consider fixed $M = 1$ and $\theta = 0.01$. We present results only for the PAM and CLARA algorithms. For the models based on tessellations, we run each algorithm for 10,000 iterations, discarding the first 2,500 iterations as burn-ins, and for the PY models,

we run the algorithms for 3,000 iterations with 1,000 burn-ins. To evaluate predictive performance, we computed the co-clustering matrices for each layer i whose entries $s_{jk}^{(i)}$ are given by $s_{jk}^{(i)} = P(z_{ij} = z_{ik} | \mathbf{D}^{(1)}, \mathbf{D}^{(2)})$, which are estimated from the MCMC output. The cluster estimate is obtained through the SALSO algorithm (Dahl et al., 2022) by minimizing the posterior expectation of the variation of information distance between the posterior samples and the cluster estimate (Dahl et al., 2022).

We consider simulated multi-view data with two layers to evaluate the performance of the six models. For both layers, we generate 100 points from a mixture of ten multivariate Gaussian distributions with cluster centers at the vertices of a standard 10-simplex and covariance matrices $\sigma_s^2 I_d$, for $\sigma_s \in \{0.1, 0.2, 0.3\}$ (larger σ_s means more cluster overlap). The cluster allocations are drawn from a Dirichlet prior with $M = 10$ for the first layer. Then, we randomly select $\lfloor 100\alpha_s \rfloor$ objects for the second layer to have the same cluster allocations as the first layer for $\alpha_s \in \{0, 0.25, 0.5, 0.75, 1\}$ (larger α_s means more similarity between layers). Finally, the cluster allocations for the remaining $100 - \lfloor 100\alpha_s \rfloor$ of the second layer is a random permutation of the cluster allocations of the first layer. For each simulation scenario, we consider 100 replicates.

We first focus on the independent Pitman-Yor (PY) model, independent tessellation models, and K-medoids. Figure 2 illustrates the median ARI between the true clustering and the cluster estimates for these models across various values of σ_s and likelihood configurations. There are no substantial differences across varying α_s since the models assume independent partitions. As anticipated, increased cluster overlap (higher σ_s) results in poorer retrieval of the clustering structure. However, the key findings are as follows: a) overall, the Bayesian models significantly outperform K-medoids (PAM and CLARA), b) the inclusion of a repulsion term in the likelihood function enhances identifiability for all Bayesian models, and c) tessellation models with a “linear” likelihood perform only slightly worse compared to tessellation models with a “double” likelihood. Notably, the independent tessellation model with linear likelihood and repulsion term stands out, demonstrating effective clustering with linear computational complexity in N per MCMC iteration. Table 2 presents the median elapsed times.

Figure 2 shows similar results for the joint models. Our key observations are as follows: a) The joint tessellation models perform comparably to or better than the joint Pitman-Yor

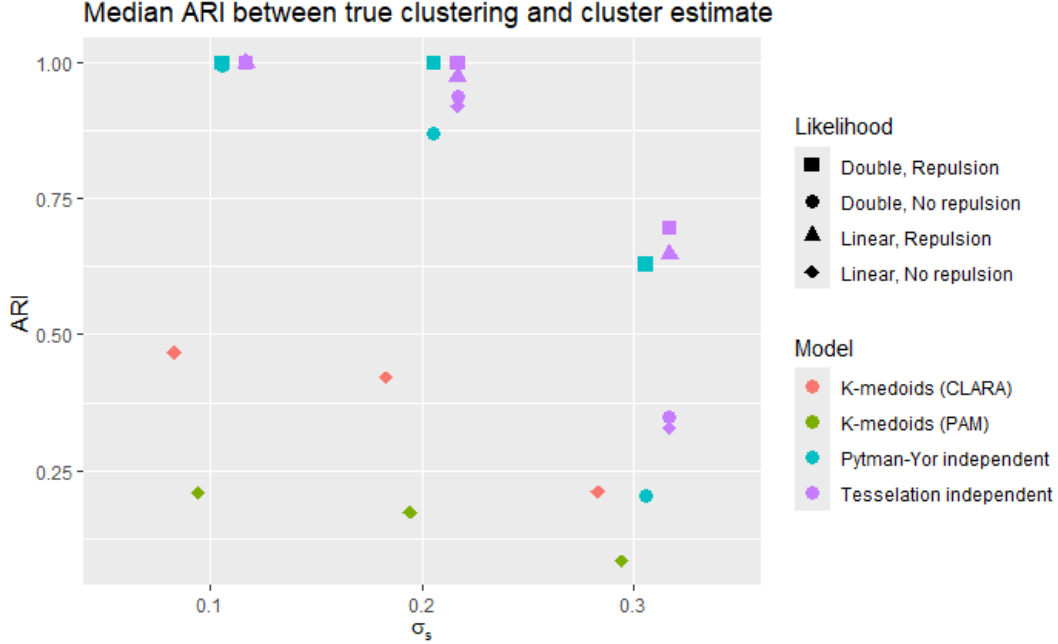


Figure 2: Median ARI between the true clustering and cluster estimates for different σ_s , models and likelihood configurations.

	PY indep.		Tessellation indep.				K-medoids
Likelihood	Double	Double	Double	Double	Linear	Linear	Linear
Repulsion	Yes	No	Yes	No	Yes	No	No
Median Time (s)	856	286	6	5	3	3	< 1

Table 2: Median elapsed time for different models and likelihood configurations. K-medoids stands for both the PAM and CLARA algorithms.

models, b) within the joint models, the “quadratic” likelihood configuration with repulsion term yields superior results, and c) the nested tessellation model exhibits poorer performance for smaller values of α_s . This decline in performance is attributed to the fact that the clustering structure of the simulated data is not nested when $\alpha_s < 1$, causing the second layer to be inadequately represented.

5 Numismatics application

Natarajan et al. (2023) and Harris et al. (2023) emphasize the necessity and importance of



Figure 3: Median ARI between the true clustering and cluster estimates for different σ_s , models and likelihood configurations.

scalable clustering methods in die studies. A die is a stamp often made of a metal piece, used to strike impressions on heated metal to form a recognizable coin. Die studies are essential for determining the number of dies used to mint a specific issue of coinage. Since dies were typically destroyed by their makers after wearing out, die studies rely on analyzing the coins produced by them. Thus, the primary task is clustering coins to identify those struck from the same die. This process is indispensable for understanding premodern historical chronology, economic conditions, including estimating mint outputs, and political history, especially in cases where corresponding historical sources are abundant, such as ancient Rome (Howgego, 2002). Numismatic research remains time-consuming, as each coin must be visually compared to every other coin to confirm die matches. For instance, the 521 coins obverses and reverses in this application would require about 550000 visual comparisons, which could require expert numismatics about 800 hours of visual inspection. This complexity hinders large-scale die studies, and thus, automatic workflows for clustering coins into different dies are needed (see Figure 5 for a visualization of the workflow).

Figure 4 shows photographs of the obverse and reverse of 98% silver coins, which were originally minted in the Pyu-Mon polities of northern and central Myanmar between the 4th and 9th centuries AD (Wicks, 1992). A total of 521 coins were collected. The obverse of each coin depicts the motif of a “Rising Sun” surrounded by a border of 27 zodiac-inspired

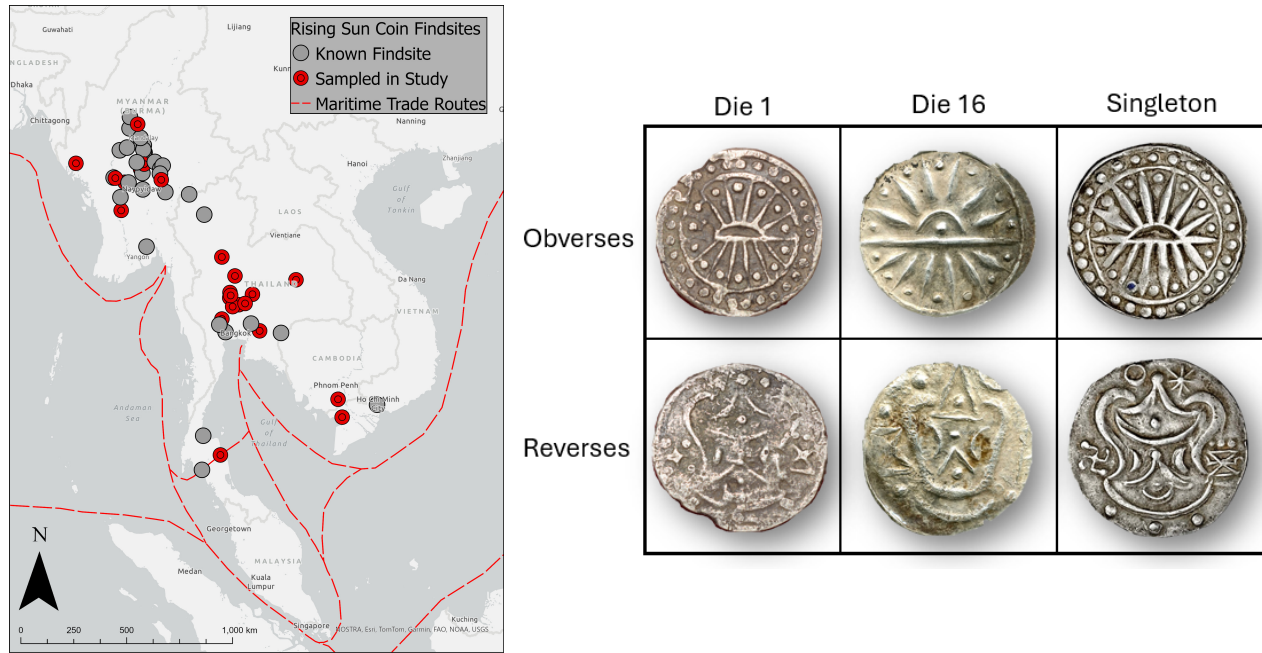


Figure 4: Map with findsites and trade routes (left) and photographs of coin obverses and reverses for several identified dies (right).

beads, while the reverse layers an Indic symbol known as a Srivatsa and other supporting symbols such as a swastika, bhadrapittha (royal throne), and celestial symbols (Gutman, 1978). “Rising Sun” coins in full-unit ($\approx 9.2 - 9.4\text{g}$) and smaller denominations have been discovered in 1st millennium AD settlements across mainland and peninsular Thailand, the Mekong Delta areas of Cambodia and Vietnam, and numerous sites throughout Myanmar (Mahlo and Margolis, 2012). Regional variations in size, weight, and quality, despite the relative uniformity of the imagery, are not only thought to reflect centralized production but also local replication and the use of these coins in interregional trade. Figure 4 illustrates known Rising Sun coin find-sites in relation to hypothesized maritime trade routes, while also highlighting the specific find-sites from which the coins used in this study were sourced. The coins were found in Myanmar, Cambodia, Thailand, and Vietnam. The majority of these coins are held in museum collections in each country (Epinal, 2014; Galloway, 2022; Malleret, 1963; Onwimol, 2019), but have also been sourced from private collections and auction houses in Europe and North America, where provenance is not as reliable (Mahlo and Margolis, 2012; Mitchiner, 1998).

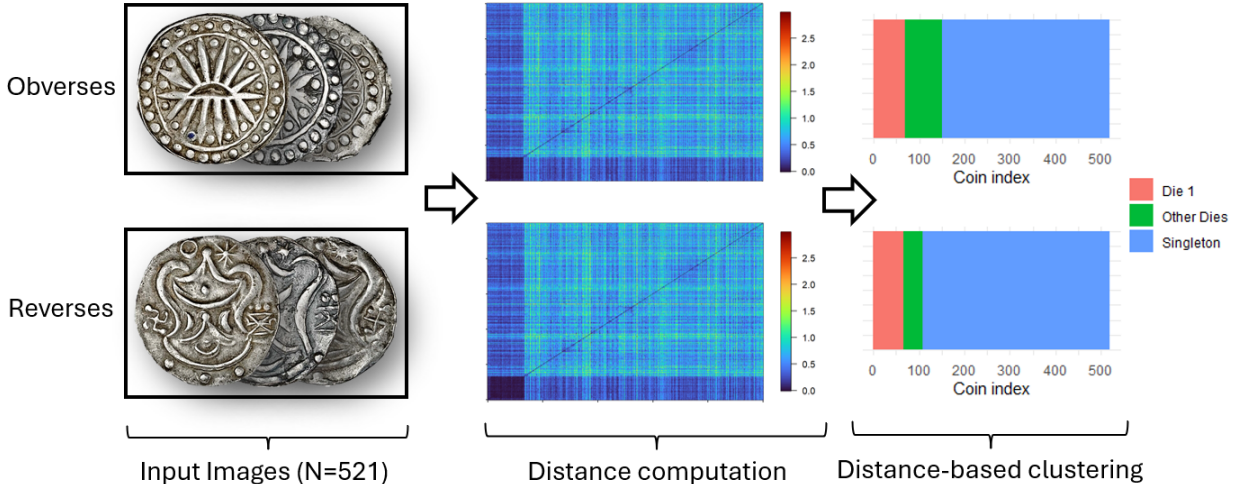


Figure 5: Workflow consisting of image preprocessing, computing the distance matrix between coins, and clustering the coins based on the distances (the cluster estimates on the right are obtained from the tessellation model with nested partitions).

5.1 Computing pairwise distances

The first challenge is computing the pairwise distances between the coins’ obverse and between the coins’ reverse based on the photographic images. These distances must capture the differences in key features that allow distinguishing between different dies. We extend the workflows developed in Natarajan et al. (2023) and Harris et al. (2023) for image preprocessing and distance matrix computation. Many coins show advanced degradation, such as rust, erosion, and missing parts, leading to large distances between coins minted by the same die. Additionally, many coins belong to singletons (die clusters with only one coin), many of which are similar to each other, thus resulting in small pairwise distances between them. These challenges led to the development of a new workflow for image preprocessing and distance computation, which builds upon the one in Harris et al. (2023) but includes several additional steps. The workflow consists of nine steps, detailed in Appendix E.1. Besides the number of key point matches between pairs of coins using the D2-Net (Dusmanu et al., 2019), we also compute local self-similarity descriptors centered on different points between pairs of coins (Shechtman and Irani, 2007) and a variety of other distance and similarity measures computed directly between the coin images. These include cosine distance, Wasserstein distance, and structural similarity index. Finally, we perform a weighted combination of these distances and similarity

measures to calculate the final distance between coin pairs. The distance matrices are shown in Figure 5.

5.2 Results

Compared to Natarajan et al. (2023) and Harris et al. (2023), we cluster the coins by eliciting a joint model for the coin obverses (layer 1) and reverses (layer 2) distances, while the previous studies only considered the coin obverse distances.

We always consider the likelihood specification with repulsion term as in (1), which leads to quadratic computational complexity, and fitted the six different models of Section 4. As detailed in Appendix E.2, we preselect 284 coins as being singleton coins and thus only perform inference on the remaining 237 coins. The criteria for preselecting a coin as a singleton is whether the 1% quantile of distances between the coin and the remaining coins is larger than 0.15, indicating that the coin differs from most other coins. Figure 6 shows the co-clustering matrices for the coin reverses for the models with dependent partition priors.

Figure 7 compares the models based on their running time and the adjusted Rand index (ARI), which measures how well the estimated clusters match the clustering structure obtained from an expert numismatist. The findings indicate that tessellation-based models, when using medoids for inference, can perform similarly to traditional Bayesian random partition models. However, they require significantly less time, reducing the running time from about five days to just a few minutes. In contrast, although extremely fast and taking only a fraction of a second to run, the K-medoids model performs poorly in estimating the true clustering structure. It achieves a low ARI, around 0.2 to 0.3, compared to the higher ARI values of approximately 0.8 to 0.9 achieved by the other models. Additional figures and results are provided in Appendix E.2.

About 13% of the coins belong to the same die, which we call Die 1; 14% of coins belong to other dies, which mostly contain two coins only, and the remaining 73% of coins belong to die clusters with only one coin (singleton). Coins from Die 1 have now been confirmed to have been cast rather than struck, a detail not initially obvious from visual inspection. Die 1 coins are found exclusively in the 4th-7th century AD at the urban center of Angkor Borei in southern Cambodia, once considered a major capital center of the so-called 1st-6th century AD “Kingdom of Funan” (Epinal, 2014). While both cast and struck coins have been found

at Angkor Borei, the interconnected port of Oc Eo in southern Vietnam, a known hub of transregional trade up to the 6th century, features exclusively struck coins amongst its known archaeological remains (Malleret, 1963). The local imitation of silver coins at Angkor Borei thus indicates the integration of this polity and its elite into a transregional trade system that valued and exchanged weighted silver coinage as either bullion or currency. The wealth reflected in coinage at Angkor Borei further indicates the incorporation of the local population into the broader economic systems of the period.

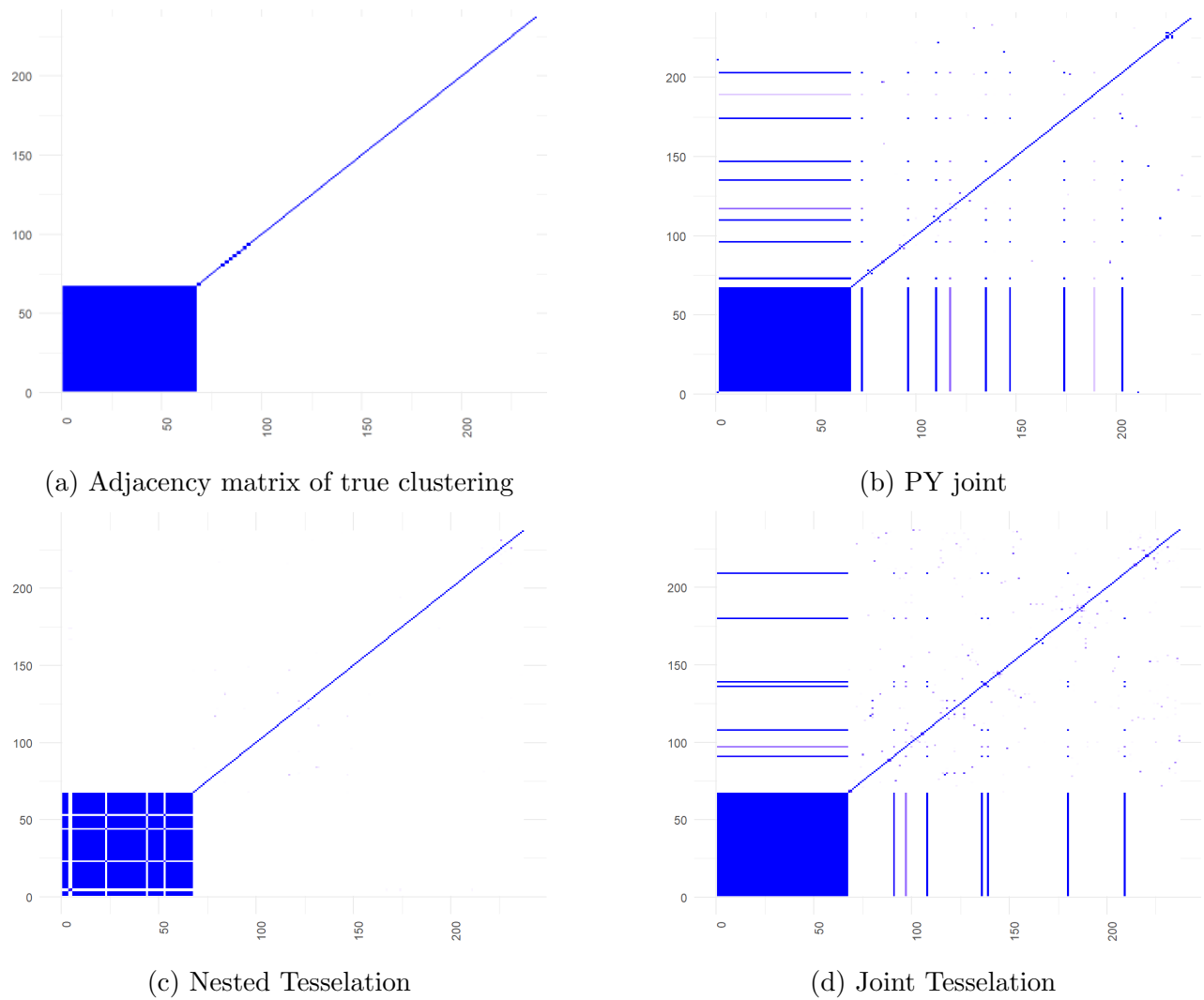


Figure 6: Posterior co-clustering matrices for selected 237 non-singleton coin reverses.

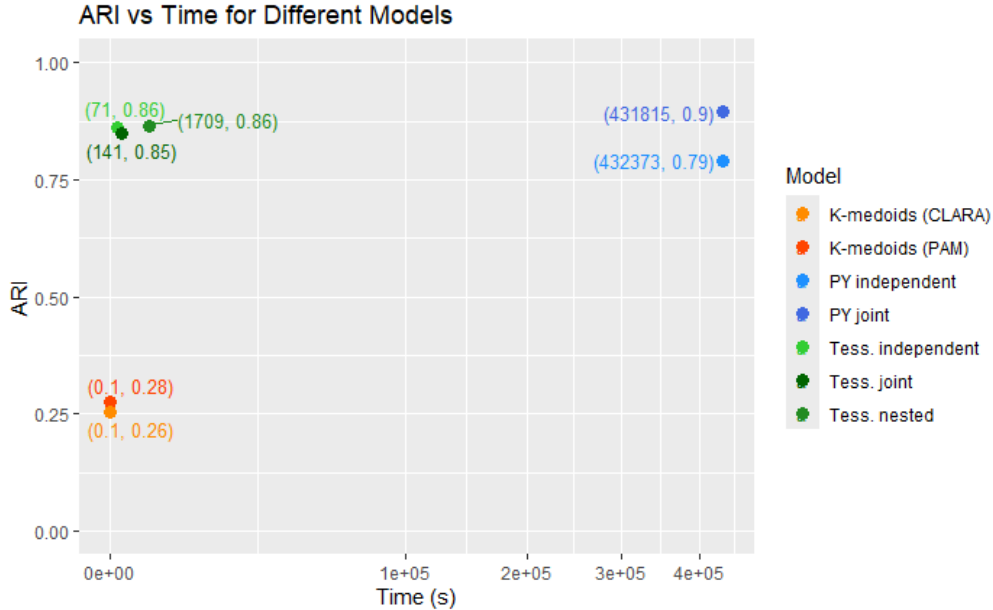


Figure 7: Adjusted Rand Index (ARI) measuring goodness-of-fit against the running time of the different algorithms (in square root scale). The reported ARI is the average of ARI_{OBV} and ARI_{REV} where ARI_{OBV} (ARI_{REV}) is the average ARI obtained between the obverses (reverses) cluster estimates and true obverse (reverse) clustering.

6 Discussion

The Bayesian distance clustering (BDC) models with partitions based on tessellations we propose in this paper can be seen as a Bayesian extension of K-medoids, where we perform probabilistic inference on the medoids set. This approach offers significant advantages over traditional Bayesian non-parametric models and traditional K-medoid algorithms. The models and corresponding MCMC algorithms presented in this work allow for more scalable inference compared to previous BDC models and other probabilistic Bayesian clustering methods while offering results with similar predictive performance. Additionally, unlike K-medoids, which provide point estimates, our Bayesian models enable the exploration of the entire posterior distribution of the medoids, leading to more robust and interpretable clustering results with better predictive power in complex datasets. Thus, these models offer a trade-off between predictive power and computational efficiency in clustering methods.

In the field of numismatics, BDC models show great promise. Automatic tools for coin clustering are crucial for historical and economic studies, as they provide insights into minting

practices and trade networks. Our models significantly reduce the time and effort required for these studies, which traditionally involve labor-intensive visual comparisons. Future work consists of performing object detection on the coins to detect symbols such as celestial objects, which are characteristic of different regions and times, thus helping to distinguish different dies. Incorporating the results of the object detection algorithms into the distance matrix is a future challenge.

Future research directions also include the development of parallel strategies and informed MCMC proposals to enhance computational efficiency in exploring the medoid set. The MCMC proposals we employ are considered “blind” as they do not utilize the information in $\pi(\mathbf{D}, \boldsymbol{\gamma})$. To obtain better proposal distributions and improve MCMC mixing, we could consider locally-balanced informed proposals (Zanella, 2019). Informed proposal algorithms are also highly parallelizable and can potentially improve our current implementation’s computational efficiency and posterior exploration.

7 Acknowledgments

This research was supported by the National University of Singapore through the grant MOE-T2EP40121-0021.

References

- Abramowitz, M. and I. A. Stegun (1948). *Handbook of mathematical functions with formulas, graphs, and mathematical tables*, Volume 55. US Government printing office.
- Bissiri, P. G., C. C. Holmes, and S. G. Walker (2016). A general framework for updating belief distributions. *Journal of the Royal Statistical Society Series B: Statistical Methodology* 78(5), 1103–1130.
- Boom, W. v. d., M. De Iorio, A. Beskos, and A. Jasra (2023). Graph Sphere: From Nodes to Supernodes in Graphical Models. *arXiv preprint arXiv:2310.11741*.
- Caron, F., W. Neiswanger, F. Wood, A. Doucet, and M. Davy (2017). Generalized Pólya Urn

- for Time-Varying Pitman-Yor Processes. *Journal of Machine Learning Research* 18(27), 1–32.
- Chatfield, K., J. Philbin, and A. Zisserman (2009). Efficient retrieval of deformable shape classes using local self-similarities. In *2009 IEEE 12th International Conference on Computer Vision Workshops, ICCV Workshops*, pp. 264–271. IEEE.
- Dahl, D. B., D. J. Johnson, and P. Müller (2022). Search algorithms and loss functions for Bayesian clustering. *Journal of Computational and Graphical Statistics* 31(4), 1189–1201.
- Dahl, D. B., R. L. Warr, and T. P. Jensen (2023). Dependent Random Partitions by Shrinking Toward an Anchor. *arXiv preprint arXiv:2312.17716*.
- De Iorio, M., S. Favaro, A. Guglielmi, and L. Ye (2019). Bayesian nonparametric temporal dynamic clustering via autoregressive Dirichlet priors. *arXiv preprint arXiv:1910.10443*.
- Denison, D., N. Adams, C. Holmes, and D. Hand (2002). Bayesian partition modelling. *Computational statistics & data analysis* 38(4), 475–485.
- Denison, D. G., C. C. Holmes, B. K. Mallick, and A. F. Smith (2002). *Bayesian methods for nonlinear classification and regression*, Volume 386. John Wiley & Sons.
- Duan, L. L. (2020). Latent simplex position model: High dimensional multi-view clustering with uncertainty quantification. *Journal of Machine Learning Research* 21(38), 1–25.
- Duan, L. L. and D. B. Dunson (2021). Bayesian distance clustering. *Journal of Machine Learning Research* 22(224), 1–27.
- Dusmanu, M., I. Rocco, T. Pajdla, M. Pollefeys, J. Sivic, A. Torii, and T. Sattler (2019). D2-net: A trainable CNN for joint description and detection of local features. In *Proceedings of the IEEE/CVF conference on computer vision and pattern recognition*, pp. 8092–8101.
- Epinal, G. (2014). *Cambodia from Funan to Chenla: A Thousand Years of Monetary History*. A National Bank of Cambodia Publication.
- Ferguson, T. S. (1973). A Bayesian analysis of some nonparametric problems. *The annals of statistics*, 209–230.

- Fraley, C. and A. E. Raftery (2002). Model-based clustering, discriminant analysis, and density estimation. *Journal of the American statistical Association* 97(458), 611–631.
- Franzolini, B., M. De Iorio, and J. Eriksson (2023). Conditional partial exchangeability: a probabilistic framework for multi-view clustering. *arXiv preprint arXiv:2307.01152*.
- Galloway, C. (2022). *Sri Ksetra Museum Collection Inventory*. De Gruyter.
- Gao, T., S. Z. Kovalsky, and I. Daubechies (2019). Gaussian process landmarking on manifolds. *SIAM Journal on Mathematics of Data Science* 1(1), 208–236.
- Gutman, P. (1978). The Ancient Coinage of Mainland Southeast Asia. *Journal of the Siam Society* 66(1), 18–21.
- Harris, A., A. Cremaschi, T. S. Lim, M. De Iorio, and K. C. Guan (2023). From Past to Future: Digital Methods Towards Artefact Analysis. *arXiv preprint arXiv:2312.13790*.
- Hastie, T., R. Tibshirani, J. H. Friedman, and J. H. Friedman (2009). *The elements of statistical learning: data mining, inference, and prediction*, Volume 2. Springer.
- Howgego, C. (2002). *Ancient history from coins*. Routledge.
- Jain, A. K. (2010). Data clustering: 50 years beyond K-means. *Pattern recognition letters* 31(8), 651–666.
- Kaufman, L. and P. J. Rousseeuw (2009). *Finding groups in data: an introduction to cluster analysis*. John Wiley & Sons.
- Maechler, M. et al. (2019). Finding groups in data: Cluster analysis extended Rousseeuw et al. *R package version 2(0)*, 242–248.
- Mahlo, D. and K. Margolis (2012). The early coins of Myanmar/Burma: messengers from the past: Pyu, Mon, and Candras of Arakan (first millenium AD). (*No Title*).
- Malleret, L. (1959-1963). *L’archéologie du Delta du Mékong*. Number 3. École française d’Extrême-Orient.
- MathWorks Inc. (2022). Matlab version: 9.13.0 (r2022b).

- Mclachlan, G. and K. Basford (1988, 01). *Mixture Models: Inference and Applications to Clustering*, Volume 38.
- Miller, J., B. Betancourt, A. Zaidi, H. Wallach, and R. C. Steorts (2015). Microclustering: When the cluster sizes grow sublinearly with the size of the data set. *arXiv preprint arXiv:1512.00792*.
- Miller, J. W. (2021). Asymptotic normality, concentration, and coverage of generalized posteriors. *Journal of Machine Learning Research* 22(168), 1–53.
- Mitchiner, M. (1998). The history and coinage of South East Asia until the fifteenth century. (*No Title*).
- Muja, M. and D. G. Lowe (2009). Fast approximate nearest neighbors with automatic algorithm configuration. *VISAPP (1)* 2(331-340), 2.
- Natarajan, A., M. De Iorio, A. Heinecke, E. Mayer, and S. Glenn (2023). Cohesion and repulsion in Bayesian distance clustering. *Journal of the American Statistical Association*, 1–11.
- Onwimol, W. (2019). *Coinage in Thailand during 4th–11th Century AD*. Ph. D. thesis, Silpakorn University.
- Paganin, S., A. H. Herring, A. F. Olshan, D. B. Dunson, and T. N. B. D. P. Study (2021). Centered partition processes: informative priors for clustering (with discussion). *Bayesian analysis* 16(1), 301.
- Page, G. L., F. A. Quintana, and D. B. Dahl (2022). Dependent modeling of temporal sequences of random partitions. *Journal of Computational and Graphical Statistics* 31(2), 614–627.
- Pitman, J. (1995). Exchangeable and partially exchangeable random partitions. *Probability theory and related fields* 102(2), 145–158.
- Pitman, J. (1996). Some developments of the Blackwell-MacQueen urn scheme. *Lecture Notes-Monograph Series*, 245–267.

- Pizer, S. M., E. P. Amburn, J. D. Austin, R. Cromartie, A. Geselowitz, T. Greer, B. ter Haar Romeny, J. B. Zimmerman, and K. Zuiderveld (1987). Adaptive histogram equalization and its variations. *Computer vision, graphics, and image processing* 39(3), 355–368.
- Rigon, T., A. H. Herring, and D. B. Dunson (2023). A generalized Bayes framework for probabilistic clustering. *Biometrika* 110(3), 559–578.
- Rudin, L. I., S. Osher, and E. Fatemi (1992). Nonlinear total variation based noise removal algorithms. *Physica D: nonlinear phenomena* 60(1-4), 259–268.
- Schubert, E. and P. J. Rousseeuw (2019). Faster k-medoids clustering: improving the PAM, CLARA, and CLARANS algorithms. In *Similarity Search and Applications: 12th International Conference, SISAP 2019, Newark, NJ, USA, October 2–4, 2019, Proceedings 12*, pp. 171–187. Springer.
- Shechtman, E. and M. Irani (2007). Matching local self-similarities across images and videos. In *IEEE conference on computer vision and pattern recognition*, pp. 1–8. IEEE.
- Wicks, R. S. (1992). *Money and Society in Ancient Burma: Mon, Pyu, and Pagan*, pp. 111–155. Cornell University Press.
- Wolfram Research Inc. (2024). Mathematica, Version 14.0.
- Xu, D. and Y. Tian (2015). A comprehensive survey of clustering algorithms. *Annals of data science* 2, 165–193.
- Zanella, G. (2019). Informed proposals for local MCMC in discrete spaces. *Journal of the American Statistical Association*.

Appendix A Marginal likelihood conditional on partition model

We can integrate out the parameters $\boldsymbol{\theta}$ and $\boldsymbol{\lambda}$ in $\pi(\mathbf{D} \mid \boldsymbol{\theta}, \boldsymbol{\lambda}, \mathcal{T})$ and avoid performing inference on these terms. First, we note that, for random variables X_i and $i = 1, \dots, N$, if $X_i \mid \lambda \stackrel{i.i.d.}{\sim}$ Gamma(δ, λ), and $\lambda \sim$ Gamma(μ, β), then

$$\int \prod_{i=1}^n \pi(x_i \mid \lambda) \pi(\lambda) d\lambda = \frac{\Gamma(\delta)^{-n} \Gamma(\mu + n\delta)}{\Gamma(\mu)} \beta^\mu \left(\prod_{i=1}^n x_i \right)^{\delta-1} \left(\beta + \sum_{i=1}^n x_i \right)^{-\mu - \delta n}$$

Therefore, $\pi(\mathbf{D} \mid \mathcal{T}) = \int \pi(\mathbf{D} \mid \boldsymbol{\theta}, \boldsymbol{\lambda}, \mathcal{T}) \pi(\boldsymbol{\lambda}) \pi(\boldsymbol{\theta}) d\boldsymbol{\lambda} d\boldsymbol{\theta}$ simplifies to

$$\begin{aligned} \pi(\mathbf{D} \mid \mathcal{T}) &= \left[\prod_{k=1}^K \int \left(\prod_{\substack{i,j \in \mathcal{C}_k \\ i < j}} f(D_{ij} \mid \lambda_k) \right) \pi(\lambda_k) d\lambda_k \right] \left[\prod_{(k,t) \in A} \int \left(\prod_{\substack{i \in \mathcal{C}_k \\ j \in \mathcal{C}_t}} g(D_{ij} \mid \theta_{kt}) \right) \pi(\theta_{kt}) d\theta_{kt} \right] \\ &= \prod_{k=1}^K \mathcal{L}_k^{(1)} \prod_{(k,t) \in A} \mathcal{L}_{kt}^{(2)} \quad \text{where} \\ \mathcal{L}_k^{(1)} &= \frac{\Gamma(\delta_1)^{-n_k^*} \Gamma(\mu + n_k^* \delta_1)}{\Gamma(\mu)} \beta^\mu \left(\prod_{\substack{i,j \in \mathcal{C}_k \\ i < j}} D_{ij} \right)^{\delta_1 - 1} \left(\beta + \sum_{\substack{i,j \in \mathcal{C}_k \\ i < j}} D_{ij} \right)^{-\mu - \delta_1 n_k^*} \\ \mathcal{L}_{kt}^{(2)} &= \frac{\Gamma(\delta_2)^{-n_k n_t} \Gamma(\zeta + n_k n_t \delta_2)}{\Gamma(\zeta)} \gamma^\zeta \left(\prod_{\substack{i \in \mathcal{C}_k \\ j \in \mathcal{C}_t}} D_{ij} \right)^{\delta_2 - 1} \left(\gamma + \sum_{\substack{i \in \mathcal{C}_k \\ j \in \mathcal{C}_t}} D_{ij} \right)^{-\zeta - \delta_2 n_k n_t} \end{aligned} \quad (12)$$

and $n_k^* = n_k(n_k - 1)/2$, and n_k is the number of objects in cluster k .

Appendix B Hyperparameter selection

The following algorithm outlines our steps to determine the hyperparameters in the distance matrix likelihood (5). The procedure is adapted from the one in Natarajan et al. (2023), which is developed for the likelihood in (1). Instead of performing maximum likelihood estimation (MLE), which requires numerical methods and is prone to numerical issues due to the potentially small dimension of \mathbf{b} (the distances between medoids), we opt for the method of moments.

Algorithm 1 Choosing $\delta_1, \delta_2, \mu, \beta$, and θ from the distance matrix \mathbf{D}

- 1: Compute an initial value for K , denoted as K_{elbow} , using the elbow method. This is achieved by applying K-medoids clustering (through the PAM, CLARA, or CLARANS algorithms) on the distance matrix \mathbf{D} for a range of K values, using the within-cluster-sum-of-squares (WSS) score as the criterion.
 - 2: Perform K-medoids clustering with K_{elbow} to obtain an initial cluster configuration.
 - 3: Define two sets of distances: \mathbf{a} , which includes distances between each non-medoid object and its assigned medoid, and \mathbf{b} , which includes distances between the medoids.
 - 4: Fit a Gamma distribution to the values in \mathbf{a} and estimate δ_1 using the method of moments, given by $\delta_1 = \bar{\mathbf{a}}^2/S_{\mathbf{a}}^2$, where $\bar{\mathbf{a}}$ and $S_{\mathbf{a}}^2$ represent the sample mean and variance of \mathbf{a} , respectively.
 - 5: Set $\mu = \delta_1 n_{\mathbf{a}}$ and $\beta = \sum_i a_i$, where $n_{\mathbf{a}}$ is the cardinality of \mathbf{a} . This corresponds to the conditional posterior of λ , obtained by specifying an improper prior $\pi(\lambda) \propto I(\lambda > 0)$ and treating \mathbf{a} as a weighted set of observations from a $\text{Gamma}(\delta_1, \lambda)$ distribution.
 - 6: Fit a Gamma distribution to the values in \mathbf{b} and estimate δ_2 and θ , the shape and rate parameters of this distribution. The method of moments yields $\delta_2 = \bar{\mathbf{b}}^2/S_{\mathbf{b}}^2$ and $\theta = \bar{\mathbf{b}}/S_{\mathbf{b}}^2$.
-

Appendix C Proofs

C.1 Proof of Proposition 1

Proof. The exchangeability property follows directly from (1) and (5). Providing a counterexample suffices to prove that the induced partition models do not generally satisfy the microclustering property.

For the second property, consider a fixed number of medoids K and a distance matrix where the distance between all objects and object 1 is a , and all remaining distances between different objects are larger than a . The resulting partition model has one large cluster comprised of $M_N = N - K + 1$ objects while the remaining $K - 1$ medoids form their own singleton clusters. It then follows that

$$\frac{M_N}{N} \rightarrow \frac{N - K + 1}{N} \neq 0$$

and thus, there is a violation of the microclustering property. \square

Appendix D Posterior inference

In this section, we present the MCMC algorithms employed to perform inference, starting with the Tessellation models for one layer in Section 2.2 of the main paper, and then presenting the algorithms for the multi-view data based on nested partitions with tessellation models, joint tessellation models, and finally Stationary dependent random partition models with EPPFs.

D.1 Tessellation models

We perform inference on the Voronoi tessellation models of Section 2.2 of the main paper using the Metropolis-Hastings (MH) algorithm, detailed in Algorithm 2. The MH algorithm involves birth, death, and move steps at each iteration. Specifically, we propose a new medoid set, γ^* , by adding, removing, or moving medoids from the medoid set of the previous iteration, $\gamma^{(t-1)}$ (Denison et al., 2002). In our implementation, we randomly choose between a birth and move step, and at every second iteration, we perform a move step.

In the birth step, we uniformly select a new index from $[N] \setminus \gamma$, representing the indices of objects that are not medoids. Similarly, for the death step, we uniformly select an index from γ to be removed. The move step combines a death step followed by a birth step. The constant β in Algorithm 2 is the ratio of the proposal probabilities (the probability of moving from the new state to the old state divided by the probability of moving from the old state to the new state).

It is also straightforward to employ a Gibbs sampler for this model. Consider the auxiliary variables w_1, \dots, w_N , where $w_i = 1$ if object i is a medoid, and $w_i = 0$ otherwise. The conditional probability is given by

$$\pi(w_i = 1 \mid \mathbf{w}_{-i}, \mathbf{D}) = \frac{\pi(w_i = 1, \mathbf{w}_{-i})\pi(\mathbf{D} \mid w_i = 1, \mathbf{w}_{-i})}{\pi(w_i = 1, \mathbf{w}_{-i})\pi(\mathbf{D} \mid w_i = 1, \mathbf{w}_{-i}) + \pi(w_i = 0, \mathbf{w}_{-i})\pi(\mathbf{D} \mid w_i = 0, \mathbf{w}_{-i})}$$

The prior $\pi(w_i = 1, \mathbf{w}_{-i})$ follows from the prior on Section 2.3 of the main paper, which only depends on N and the number of clusters $K = \sum_i^N w_i$. We add object i to the medoid set with probability given by $\pi(w_i = 1 \mid \mathbf{w}_{-i}, \mathbf{D})$, and otherwise remove it from the medoid set. At each step of the Gibbs sampler, this operation is repeated for all N objects. Thus, we increase the computational cost of each MCMC iteration by a factor of N compared to Algorithm 2. However, combining the Birth-Death and Move algorithms with the Gibbs sampler may

Algorithm 2 Birth-Death and Move Algorithm for Tesselation Models

1: Initialize parameters $\gamma^{(0)}$

2: **for** $t = 1, 2, \dots, T$ **do**

3: Sample $u \sim \text{Uniform}(0, 1)$

4: **if** $t \bmod 2 = 0$ **then**

▷ Move step

5: Remove one medoid uniformly from γ and add a new one uniformly from $[N] \setminus \gamma$ leading to γ^* and compute $\mathcal{T}^*(\mathbf{D}, \gamma^*)$ from (3)

6: Calculate the acceptance ratio:

$$\alpha = \min \left(1, \frac{\pi(\mathbf{D}|\mathcal{T}^*)\pi(\gamma^*)}{\pi(\mathbf{D}|\mathcal{T})\pi(\gamma)} \times \beta \right), \quad \beta = \frac{|\gamma^{(t-1)}|(N - |\gamma^{(t-1)}|)}{|\gamma^*|(N - |\gamma^*|)} = 1$$

7: **else if** $u < 0.5$ **then**

▷ Birth step

8: Add a new medoid uniformly from $[N] \setminus \gamma$ leading to γ^* and compute $\mathcal{T}^*(\mathbf{D}, \gamma^*)$ from (3)

9: Calculate the acceptance ratio:

$$\alpha = \min \left(1, \frac{\pi(\mathbf{D}|\mathcal{T}^*)\pi(\gamma^*)}{\pi(\mathbf{D}|\mathcal{T})\pi(\gamma)} \times \beta \right), \quad \beta = \frac{N - |\gamma^{(t-1)}|}{|\gamma^*|}$$

10: **else**

▷ Death step

11: Remove a medoid uniformly from γ leading to γ^* and compute $\mathcal{T}^*(\mathbf{D}, \gamma^*)$ from (3)

12: Calculate the acceptance ratio:

$$\alpha = \min \left(1, \frac{\pi(\mathbf{D}|\mathcal{T}^*)\pi(\gamma^*)}{\pi(\mathbf{D}|\mathcal{T})\pi(\gamma)} \times \beta \right), \quad \beta = \frac{|\gamma^{(t-1)}|}{N - |\gamma^*|}$$

13: **end if**

14: Sample $v \sim \text{Uniform}(0, 1)$

15: **if** $v < \alpha$ **then**

16: Accept the new parameters: $\gamma^{(t)} = \gamma^*$, $\mathcal{T}^{(t)} = \mathcal{T}^*$

17: **else**

18: Reject the new parameters: $\gamma^{(t)} = \gamma^{(t-1)}$, $\mathcal{T}^{(t)} = \mathcal{T}^{(t-1)}$

19: **end if**

20: **end for**

21: **Output:** $\gamma^{(1)}, \gamma^{(2)}, \dots, \gamma^{(T)}$, $\mathcal{T}^{(1)}, \mathcal{T}^{(2)}, \dots, \mathcal{T}^{(T)}$

be beneficial since the Gibbs sampler gives an acceptance rate of 1, while Algorithm 2 will generally have a low acceptance rate. Future work aims to explore this approach in greater detail.

D.2 Tessellation models for nested partitions

Algorithm 3 is an adaptation of the MCMC algorithm in Algorithm 2. In Algorithm 3, we first generate proposals for the medoid sets using the same birth, death and move steps of Algorithm 2. After generating a proposal γ_1^* , we ensure that the pair $(\gamma_1^*, \gamma_2^{(t-1)})$ is valid, as discussed in Section D.2 of the main paper. Subsequently, proposals for γ_2^* need to be generated. We could have proceeded as before and used one birth, death, or move step of Algorithm 2. However, we obtained better mixing by generating K_1 proposals and acceptance/rejection steps for γ_2 in series. For each of the K_1 clusters in layer 1, we consider a birth, death, and move step for layer two restricted to that cluster. At step j , we only add, remove, or move medoids inside \mathcal{C}_{1j} , the cluster j of layer 1, instead of $[N]$.

D.3 Joint tessellation models

Algorithm 4 is an adaptation of the MCMC algorithm in Algorithm 2. For computational efficiency, we avoid performing inference on α directly. We set the prior $\alpha \sim \text{Beta}(a, b)$ and then marginalize out α from the last three terms of the posterior density (11) of the main paper, leading to

$$\begin{aligned} C(\gamma_1, \gamma_2; \mathbf{D}^{(1)}, \mathbf{D}^{(2)}) &= \int \exp(-\phi(\alpha)d(\gamma_1, \gamma_2; \mathbf{D}^{(1)}, \mathbf{D}^{(2)}))\pi(\alpha)d\alpha \\ &= \frac{\Gamma(a)\text{T}[a, 1 - b, d(\gamma_1, \gamma_2; \mathbf{D}^{(1)}, \mathbf{D}^{(2)})]}{\beta(a, b)} \end{aligned}$$

where T stands for the Tricomi confluent hypergeometric function (Abramowitz and Stegun, 1948). Thus, (11) of the main paper simplifies to

$$\tilde{\pi}(\gamma_1, \gamma_2 | \mathbf{D}^{(1)}, \mathbf{D}^{(2)}) \propto \pi(\mathbf{D}^{(1)} | \gamma_1)\pi(\mathbf{D}^{(2)} | \gamma_2)C(\gamma_1, \gamma_2; \mathbf{D}^{(1)}, \mathbf{D}^{(2)})\pi(\gamma_1, \gamma_2)$$

After obtaining posterior samples of γ_1 and γ_2 , we then compute posterior samples of α through

$$\tilde{\pi}(\alpha | \gamma_1, \gamma_2, \mathbf{D}^{(1)}, \mathbf{D}^{(2)}) \propto \exp(-\phi(\alpha)d(\gamma_1, \gamma_2; \mathbf{D}^{(1)}, \mathbf{D}^{(2)}))(1 - \alpha)^{b-1}\alpha^{a-1}$$

Algorithm 3 Birth-Death and Move Algorithm for Tessellation Models

```
1: Initialize parameters  $\gamma_1^{(0)}$  and  $\gamma_2^{(0)}$ 
2: for  $t = 1, 2, \dots, T$  do

    // Update the first layer
3:   Generate  $\gamma_1^*$  and  $\mathcal{T}_1^*$  from steps 3-16 of Algorithm 2 (using matrix  $\mathbf{D}^{(1)}$ )
4:   Set  $\gamma_2^* = \gamma_2^{(t-1)}$ 

    // Guarantee that medoid sets are valid
5:   for  $i = 1, 2, \dots, K_1$  do
6:     if  $\gamma_2 \cap \mathcal{C}_{iz_{1j}} = \emptyset$  then                                 $\triangleright$  Layer 2 has no medoids at cluster  $\mathcal{C}_{iz_{1j}}$ 
7:       Add the medoid  $z_{1j}$  to  $\gamma_2^*$                                  $\triangleright$  medoid of the cluster of object  $j$  at Layer 1
8:     end if
9:   end for
10:  Accept or reject  $\gamma_1^*$  and  $\gamma_2^*$  and obtain  $\gamma_1^{(t)}, \mathcal{T}_1^{(t)}, \gamma_2^{(t)}$  and  $\mathcal{T}_2^{(t)}$ 

    // Update the second layer cycling through each cluster of the first layer
11:  for  $i = 1, 2, \dots, K_1$  do
12:    Generate  $\gamma_2^*$  and  $\mathcal{T}_2^*$  from steps 3-16 of Algorithm 2 (using matrix  $\mathbf{D}^{(2)}$  and (10))
    but consider:

    Birth Step: uniformly add a medoid in  $\mathcal{C}_{1i} \setminus \gamma_2$  (instead of  $[N] \setminus \gamma_2$ )

    Death Step: uniformly remove medoids in  $\mathcal{C}_{1i} \cap \gamma_2$  (instead of  $\gamma_2$ )

    Move Step: Death step followed by a birth step

13:    Accept or reject  $\gamma_2^*$  and obtain  $\gamma_2^{(t)}$  and  $\mathcal{T}_2^{(t)}$ 
14:  end for
15: end for
16: Output:  $\gamma_1^{(1)}, \gamma_2^{(1)}, \dots, \gamma_1^{(T)}, \gamma_2^{(T)}, \mathcal{T}_1^{(1)}, \mathcal{T}_2^{(1)}, \dots, \mathcal{T}_1^{(T)}, \mathcal{T}_2^{(T)}$ 
```

A Gibbs sampler can also be employed by considering the auxiliary variables $w_{i,j}$ for $i \in \{1, 2\}$ and $j \in [N]$, where $w_{i,j}$ equals one if object j at layer i is a medoid and is zero

Algorithm 4 Birth-Death and Move Algorithm for Joint Tessellation Models

- 1: Initialize parameters $\gamma_1^{(0)}$ and $\gamma_2^{(0)}$
- 2: **for** $t = 1, 2, \dots, T$ **do**
- 3: Generate γ_1^* , \mathcal{T}_1^* and β from steps 3-16 of Algorithm 2 (using matrix $\mathbf{D}^{(1)}$)
- 4: Compute the acceptance probability:

$$\alpha_1 = \min \left(1, \frac{\pi(\mathbf{D}^{(1)} | \mathcal{T}_1^*) C(\gamma_1^*, \gamma_2^{(t-1)}; \mathbf{D}^{(1)}, \mathbf{D}^{(2)}) \pi(\gamma_1^*)}{\pi(\mathbf{D}^{(1)} | \mathcal{T}_1^{(t-1)}) C(\gamma_1^{(t-1)}, \gamma_2^{(t-1)}; \mathbf{D}^{(1)}, \mathbf{D}^{(2)}) \pi(\gamma_1^{(t-1)})} \times \beta \right)$$

- 5: Set $\gamma_1^{(t)} = \gamma_1^*$ and $\mathcal{T}_1^{(t)} = \mathcal{T}_1^*$ with probability α_1 . Otherwise set $\gamma_1^{(t)} = \gamma_1^{(t-1)}$ and $\mathcal{T}_1^{(t)} = \mathcal{T}_1^{(t-1)}$
- 6: Generate γ_2^* , \mathcal{T}_2^* and β from steps 3-16 of Algorithm 2 (using matrix $\mathbf{D}^{(2)}$)
- 7: Compute the acceptance probability:

$$\alpha_2 = \min \left(1, \frac{\pi(\mathbf{D}^{(2)} | \mathcal{T}_2^*) C(\gamma_1^{(t)}, \gamma_2^*; \mathbf{D}^{(1)}, \mathbf{D}^{(2)}) \pi(\gamma_2^*)}{\pi(\mathbf{D}^{(2)} | \mathcal{T}_2^{(t-1)}) C(\gamma_1^{(t)}, \gamma_2^{(t-1)}; \mathbf{D}^{(1)}, \mathbf{D}^{(2)}) \pi(\gamma_2^{(t-1)})} \times \beta \right)$$

- 8: Set $\gamma_2^{(t)} = \gamma_2^*$ and $\mathcal{T}_2^{(t)} = \mathcal{T}_2^*$ with probability α_2 . Otherwise set $\gamma_2^{(t)} = \gamma_2^{(t-1)}$ and $\mathcal{T}_2^{(t)} = \mathcal{T}_2^{(t-1)}$
 - 9: **end for**
 - 10: **Output:** $\gamma_1^{(1)}, \gamma_2^{(1)}, \dots, \gamma_1^{(T)}, \gamma_2^{(T)}, \mathcal{T}_1^{(1)}, \mathcal{T}_2^{(1)}, \dots, \mathcal{T}_1^{(T)}, \mathcal{T}_2^{(T)}$
-

otherwise. The Gibbs sampler is based on the following full conditional probabilities

$$\pi(w_{1,i} = 1 \mid \mathbf{w}_{1,-i}, \mathbf{w}_2, \mathbf{D}^{(1)}, \mathbf{D}^{(2)}) = \frac{a}{a+b}$$

$$a = \pi(w_{1,i} = 1, \mathbf{w}_{1,-i}) \pi(\mathbf{D}^{(1)} \mid w_{1,i} = 1, \mathbf{w}_{1,-i}) C(w_{1,i} = 1, \mathbf{w}_{1,-i}, \mathbf{w}_2; \mathbf{D}^{(1)}, \mathbf{D}^{(2)})$$

$$b = \pi(w_{1,i} = 0, \mathbf{w}_{1,-i}) \pi(\mathbf{D}^{(1)} \mid w_{1,i} = 0, \mathbf{w}_{1,-i}) C(w_{1,i} = 0, \mathbf{w}_{1,-i}, \mathbf{w}_2; \mathbf{D}^{(1)}, \mathbf{D}^{(2)})$$

and

$$\pi(w_{2,i} = 1 \mid \mathbf{w}_{2,-i}, \mathbf{w}_1, \mathbf{D}^{(1)}, \mathbf{D}^{(2)}) = \frac{a}{a+b}$$

$$a = \pi(w_{2,i} = 1, \mathbf{w}_{2,-i}) \pi(\mathbf{D}^{(2)} \mid w_{2,i} = 1, \mathbf{w}_{2,-i}) C(\mathbf{w}_1, w_{2,i} = 1, \mathbf{w}_{2,-i}; \mathbf{D}^{(1)}, \mathbf{D}^{(2)})$$

$$b = \pi(w_{2,i} = 0, \mathbf{w}_{2,-i}) \pi(\mathbf{D}^{(2)} \mid w_{2,i} = 0, \mathbf{w}_{2,-i}) C(\mathbf{w}_1, w_{2,i} = 0, \mathbf{w}_{2,-i}; \mathbf{D}^{(1)}, \mathbf{D}^{(2)})$$

D.4 Stationary dependent random partition models with EPPFs

Here, we overview the main steps in performing inference in stationary and dependent random partition models. For more details, see Page et al. (2022). First, we have,

$$\pi(\mathcal{T}_2|\mathcal{T}_1, \boldsymbol{\kappa}) = \frac{\pi(\mathcal{T}_2)}{\pi(\mathcal{T}_2^{\mathcal{R}})} I[\mathcal{T}_1^{\mathcal{R}} = \mathcal{T}_2^{\mathcal{R}}]$$

where $\mathcal{R} = \{i : \kappa_i = 0\}$ contains the indexes of the objects that are not subject to reassignment, and $\mathcal{T}_2^{\mathcal{R}}$ is the subset of \mathcal{T}_2 that contains the objects that are not subject to reassignment. Then, the full conditional for κ_i is given by

$$\pi(\kappa_i|-) = \frac{\alpha}{\alpha + (1 - \alpha) \Pr(\mathcal{T}_2^{\mathcal{R}^{(+i)}}) / \Pr(\mathcal{T}_2^{\mathcal{R}^{(-i)}})} I[\mathcal{T}_1^{\mathcal{R}^{(+i)}} = \mathcal{T}_2^{\mathcal{R}^{(+i)}}] \quad (13)$$

where $\mathcal{T}_2^{\mathcal{R}^{(+i)}}$ and $\mathcal{T}_2^{\mathcal{R}^{(-i)}}$ is the cluster $\mathcal{T}_2^{\mathcal{R}}$ including and excluding the object i , respectively. For the cluster allocation labels \mathbf{z}_2 , we only update the elements j that are subject to reallocation, i.e., $j : \kappa_j = 0$, according to

$$\pi(z_{2,j} = k|-) \propto \pi(\mathbf{D}^{(2)}|z_{2,j} = k, \mathbf{z}_{2,-j})\pi(z_{2,j} = k, \mathbf{z}_{2,-j}) \quad k = 1, \dots, K_2^{(-i)} + 1 \quad (14)$$

where $K_2^{(-i)}$ is the number of clusters in layer two if we remove object i . The first density on the right-hand side is given by (12), and the second density can be calculated from the EPPF. To update $z_{1,j}$, we ensure that when reallocating object j to cluster k , obtaining the new partition $\mathcal{T}_{1,z_{1,j}=k}$, we preserve compatibility with \mathcal{T}_2 , in the sense that \mathcal{T}_2 can be obtained from $\mathcal{T}_{1,z_{1,j}=k}$ by only updating the objects j where $\kappa_j = 1$. Thus, the full conditional is

$$\pi(z_{1,j} = k|-) \propto \pi(\mathbf{D}^{(1)}|z_{1,j} = k, \mathbf{z}_{1,-j})\pi(z_{1,j} = k, \mathbf{z}_{1,-j}) I[\mathcal{T}_{1,z_{1,j}=k}^{\mathcal{R}} = \mathcal{T}_2^{\mathcal{R}}] \quad k = 1, \dots, K_1^{(-i)} + 1 \quad (15)$$

We set the prior $\alpha \sim \text{Beta}(a, b)$, and so the full conditional for α is

$$\pi(\alpha|-) \propto \text{Beta}\left(a + \sum_i \kappa_i, b + N - \sum_i \kappa_i\right) \quad (16)$$

We fixed M and θ in the main application and simulations, so no inference was performed in these parameters. Finally, we implemented a Gibbs sampler based on the full conditionals (13), (14), (15), and (16), to obtain posterior samples for $\mathcal{T}_1, \mathcal{T}_2, \boldsymbol{\kappa}$, and α .

Appendix E Numismatics application

E.1 Workflow for image preprocessing and distance computation

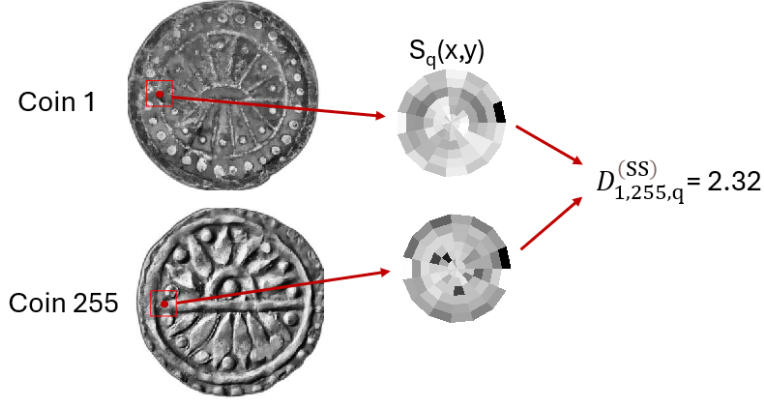


Figure 8: We show the self-similarity descriptors $S_q(x, y)$ in polar coordinates centered on the red dot for two coins and the Euclidian distance between those two descriptors.

Besides the D2-Net (Dusmanu et al., 2019) employed in Harris et al. (2023) to match key points between the two coins, we also compute local self-similarity descriptors. Figure 8 shows the self-similarity descriptor for a given pixel q . A surrounding image region centered at q (with a radius of 40 pixels) is compared with the inner region patch of 5-pixel radius centered on q using the sum of square differences (SSD) in the color space. The resulting distance surface $SSD_q(x, y)$ is normalized to form a “correlation surface” $S_q(x, y)$:

$$S_q(x, y) = \exp \left(-\frac{SSD_q(x, y)}{\max(\text{var}_{\text{noise}}, \text{var}_{\text{auto}}(q))} \right) \quad (17)$$

where $\text{var}_{\text{noise}}$ is a constant for acceptable photometric variations and $\text{var}_{\text{auto}}(q)$ accounts for the pattern structure and contrast at q . This ensures that sharp edges are more tolerant to pattern variations than smooth patches. The correlation surface $S_q(x, y)$ is then converted into log-polar coordinates centered at q and divided into 90 bins (15 angles, six radial intervals). The maximum correlation value in each bin forms the descriptor vector d_q , normalized to a range of $[0, 1]$ to measure the similarity between patches while considering geometric and photometric variations. More details about this descriptor can be found in Shechtman and Irani (2007). Afterward, we compute the Euclidean distance between the descriptor centered on q between coins i and j , leading to the distance $D_{i,j,q}^{(SS)}$.

We detail next the workflow for image preprocessing and distance computation of Section 5 of the main paper. We mainly utilize the R programming language, but steps 3,4, and 6 are performed in Mathematica Wolfram Research Inc. (2024), and steps 1, 2, 5, and 7 are performed in Matlab MathWorks Inc. (2022). The workflow is based on the workflow in Harris et al. (2023), but we add steps 3, 4, 5, 6, and 8. We apply the preprocessing steps (1 to 5) and distance computation steps (6 to 9) separately for the coin obverse and reverses, and the steps are

1. *Conversion and Resizing:* We transform all images to grayscale and standardize their dimensions to 300x300 pixels.
2. *Noise Reduction and Restoration:* We perform total-variation image restoration Rudin et al. (1992) on each image to mitigate noise generated during image acquisition due to low lighting conditions. This process helps to smooth out minor imperfections while maintaining the sharpness of edges and corners. Next, we use contrast-limited adaptive histogram equalization (Pizer et al., 1987) to enhance local contrast and edge definition. Total-variation restoration is applied once more to address any artifacts these local transformations introduce.
3. *Background Removal:* We employ the `RemoveBackground` function in Mathematica to isolate the coins from the background.
4. *Image Alignment:* We align the images by minimizing the mean squared error between the coin images and the reference coin image (the first one in the dataset). We utilize the `ImageAlign` function in Mathematica with a mean square gradient descent method. The image alignment is necessary for steps 6 and 8.
5. *Color histogram adjustment:* We adjust the histograms of each coin image to match the reference image, standardizing brightness and contrast across the dataset (needed for step 6). We employ the function `imhistmatch` in Matlab.
6. *Direct Distance and Similarity Measures:* We compute a variety of direct distances and similarity measures between the coin images, such as Euclidean distance, cosine distance, mean pattern intensity, gradient correlation, structural similarity index (SSIM),

Wasserstein distance, and mutual information variation. These measures are computed using the `ImageDistance` function in Mathematica.

7. *D2-Net model*: The D2-Net model incorporates a 16-layer VGG16 convolutional neural network to detect and describe key points within the coin images that characterize their visual attributes. D2-Net yields a representation of the coin image that is simultaneously a detector (i.e., a locator of key points in the image) and a descriptor (i.e., represented by an array of features describing the image properties at the corresponding key points). A detailed introduction and implementation guidance of the D2-Net model are in Dusmanu et al. (2019). Following the feature extraction at the matched key points, the images are paired and analyzed using an efficient approach to nearest neighbor search (Muja and Lowe, 2009). This process matches landmarks identified among the D2-Net key points across different coin images. The procedure includes using Gaussian Processes landmarking (Gao et al., 2019) to rank the reliability of these landmarks for image comparison. From this procedure, we obtain the number of matches between coin images i and j (with a larger number of matches related to larger similarities), $S_{i,j}^{(D2)}$.
8. *Local self-similarity descriptors*: We employ the “local self-similarity descriptors” in Shechtman and Irani (2007), which captures internal geometric patterns within images while accounting for small local affine deformations. It captures self-similarity of edges, repetitive patterns, and complex textures in a single unified way. For each coin image, we compute these descriptors in 3600 equally spaced locations, obtaining a vector $\mathbf{v}_{i,q}$, which is the descriptor at location q of image i . We employ the C++ implementation in Chatfield et al. (2009). Since the images have been aligned, we can directly compute the Euclidean distances between the descriptors of coin i and j at location q : $D_{i,j,q}^{(SS)} = \|\mathbf{v}_{i,q} - \mathbf{v}_{j,q}\|_2$.
9. *Compute the final distances*: From the previous three steps, we obtain a variety of distances and similarity measures for each coin pair. We now have to select which similarities/distances are most relevant and how to weigh them appropriately. The similarity measures are given a negative weight (higher similarity means smaller distance). Most of the self-similarity descriptors $D_{i,j,l}^{(SS)}$ are not relevant since they pertained to locations outside the coins or locations inside the coins with slight variation between coin pairs.

Distance/Similarity	Weight
Number of Matches in D2-Net	-8
SSIM	+7
Self-similarity descriptor at location 56	+4
Self-similarity descriptor at location 306	+4
Mean Pattern Intensity	-3
Gradient correlation	-2

Table 3: Weights used to compute the final distances of the coin obverses (rounded weights).

To select the best distances and similarity measures, we consider a subset of 50 coins. We fit a logistic regression model with a Lasso penalty, where the response is one if a coin pair was in the same die (or 0 otherwise), and the covariates are all the distances and similarities computed for each coin pair. The fitted regression coefficients from the logistic regression inform which of the distances/similarities are the most relevant, also allowing us to adequately compute the weight of each distance/similarity measure. Finally, from the weights in Table 3 and 4, we compute the final distances between each coin pair (for the obverses and the reverses) by doing the weighted average of all the distances and similarity measures. After obtaining the final distance matrix \mathbf{D} , we further standardized it to obtain $\tilde{\mathbf{D}}$. Subsequently, we apply the transformation $Q(\Phi(D_{ij}))$, where Q is the quantile function of the Gamma distribution with a shape parameter of 3 and a rate parameter of 5. This final transformation is performed to ensure that the histograms of the distances would resemble a Gamma distribution more closely (see Figure 9). This transformation enhances the fit to the model described in (1) and (5), which assumes a Gamma distribution.

E.2 Additional results and figures for the numismatics application

This section presents supplementary results and figures pertinent to the numismatics application discussed in Section 5. Figure 9 illustrates the 1% quantile of the pairwise distances between an individual coin and all other coins. A high 1% quantile indicates that a coin is potentially very different from most other coins, suggesting it could belong to a singleton

Distance/Similarity	Weight
Cosine Distance	+11
Number of Matches in D2-Net	-8
SSIM	+7
Normalized Mutual Variation Information	+5
Self-similarity descriptor at location 63	+4
Self-similarity descriptor at location 199	+4

Table 4: Weights used to compute the final distances of the coin reverses (rounded weights).

cluster.

Prior to conducting the analysis, it was anticipated that the majority of coins in this application would be singletons and should not be clustered with any other coins. Consequently, a threshold for the 1% quantile of the pairwise distances was established to classify a coin as belonging to a singleton cluster or not. After that, we employ the clustering algorithm exclusively for the non-singleton coins. This approach reduces the dimensionality of the problem and enhances the performance of the clustering algorithm. Initially, the 1% quantile of the pairwise distances was modeled using a mixture of two Gamma distributions. Figure 9 shows that the two groups suggest a demarcation between non-singleton and singleton coins at approximately 0.07. However, a threshold of 0.15 is selected to adopt a more conservative approach.

Table 5 summarizes each model’s posterior number of clusters, running time, and the adjusted Rand index (ARI) between the true clustering structure and the cluster estimate (considering all coins). In Figure 10, we show the true adjacency matrices for the coin obverses and reverses, and Figure 7 and 6 show the posterior co-clustering matrices for the independent and joint models, respectively. Finally, Figure 11 shows the posterior distribution of the dependency parameter α for the joint PY and tessellation models, where the posterior median was 0.98 and 0.83, respectively.

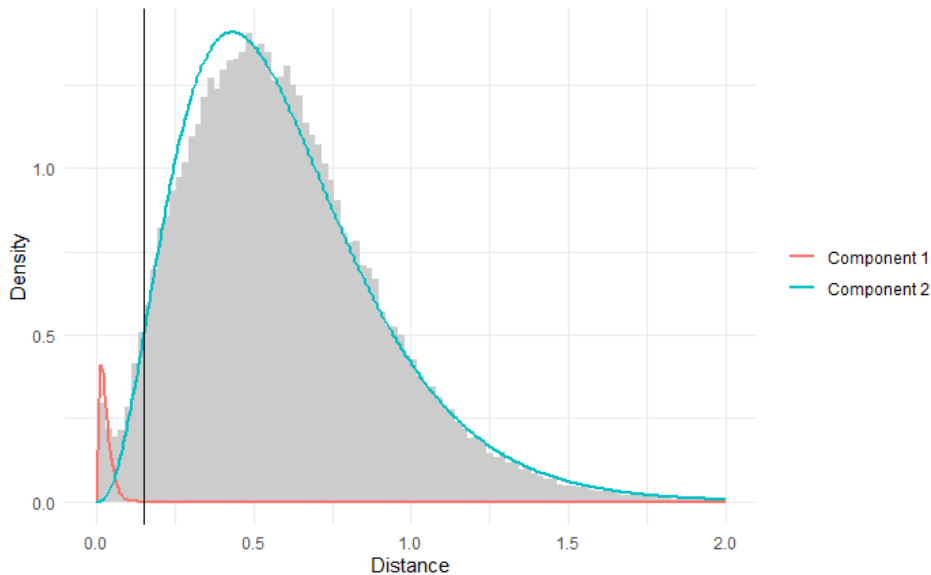


Figure 9: Mixture of Gamma distributions fit (blue and red curves) to the observed average pairwise distance from one coin to the other coins (grey histogram). The black vertical line indicates the chosen threshold. Coins whose average distance to other coins is above the threshold are classified as singleton coins.

Model	Layer	ARI	K	Time
K-medoids (PAM)	1	0.24	398 (fixed)	< 1 s
K-medoids (PAM)	2	0.31	398 (fixed)	< 1 s
K-medoids (CLARA)	1	0.24	398 (fixed)	< 1 s
K-medoids (CLARA)	2	0.27	398 (fixed)	< 1 s
PY independent	1	0.79	426 (0.53)	19178 s
PY independent	2	0.79	416 (2.12)	15296 s
PY joint	1	0.93	435 (0.62)	\approx 5 days
PY joint	2	0.86	435 (1.02)	\approx 5 days
Tesselation independent	1	0.92	405 (2.39)	69 s
Tesselation independent	2	0.80	405 (3.35)	72 s
Tesselation nested	1	0.82	399 (2.85)	1709 s
Tesselation nested	2	0.91	437 (1.25)	1709 s
Tesselation joint	1	0.89	395 (2.82)	141 s
Tesselation joint	2	0.81	407 (2.15)	141 s

Table 5: Adjusted Rand Index (ARI) between the cluster estimates and true clustering, posterior mean (and standard) deviation of the number of clusters K , and running time of the algorithms for coin obverses (layer 1) and coin reverses (layer 2).

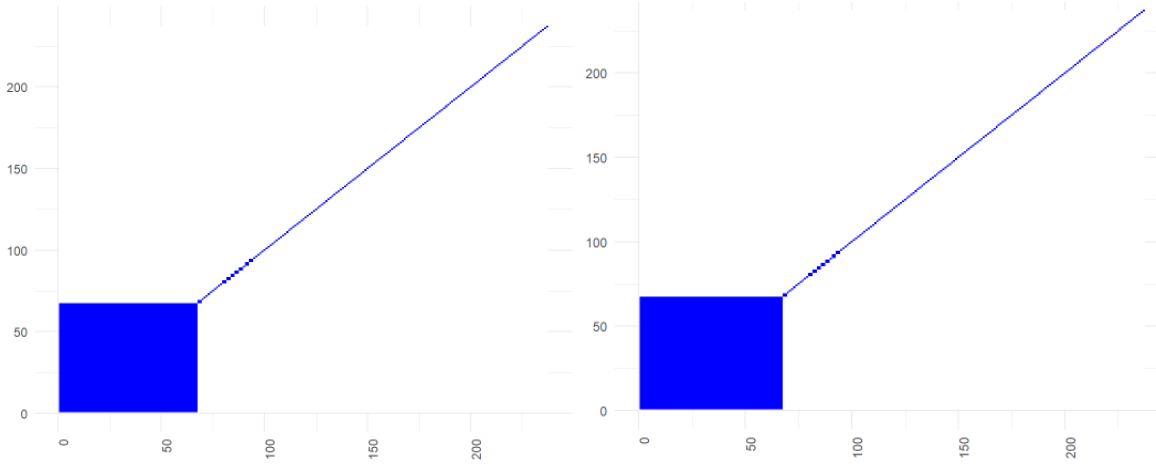


Figure 10: Adjacency matrix of the true clusters for obverses (left) and reverses (right).

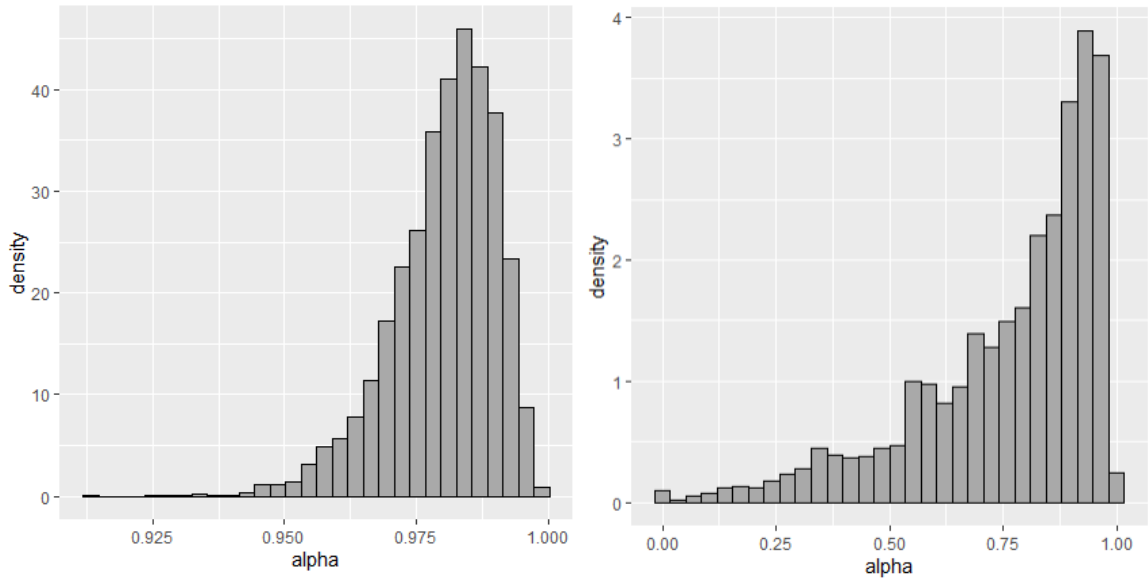


Figure 11: Dependency parameter α for the joint PY model (left) and joint tessellation model (right).

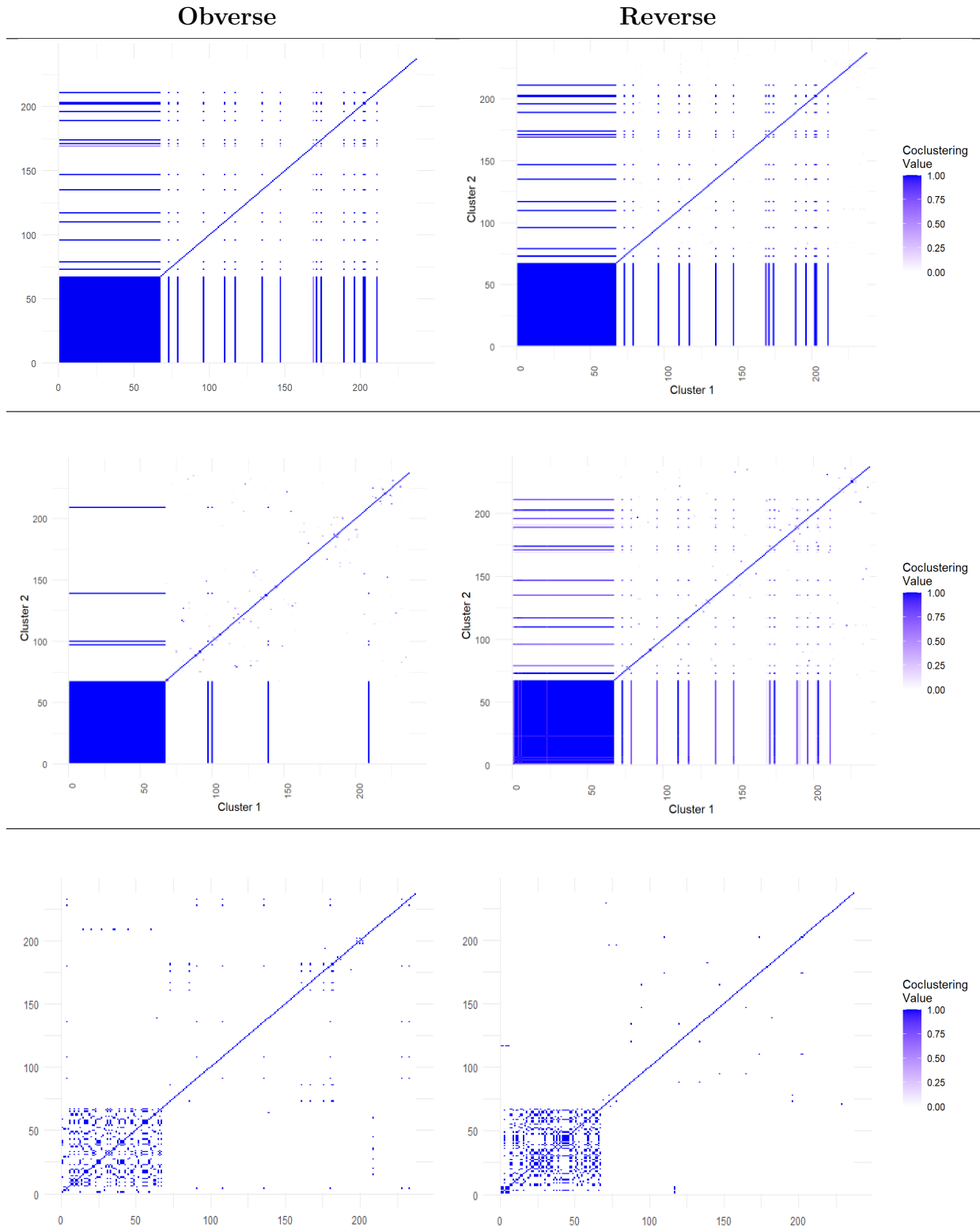


Table 6: Co-clustering matrices for the obverses and reverses for the independent Pitman-Yor model (first row), independent tessellation model (second row), and the PAM algorithm (third row).

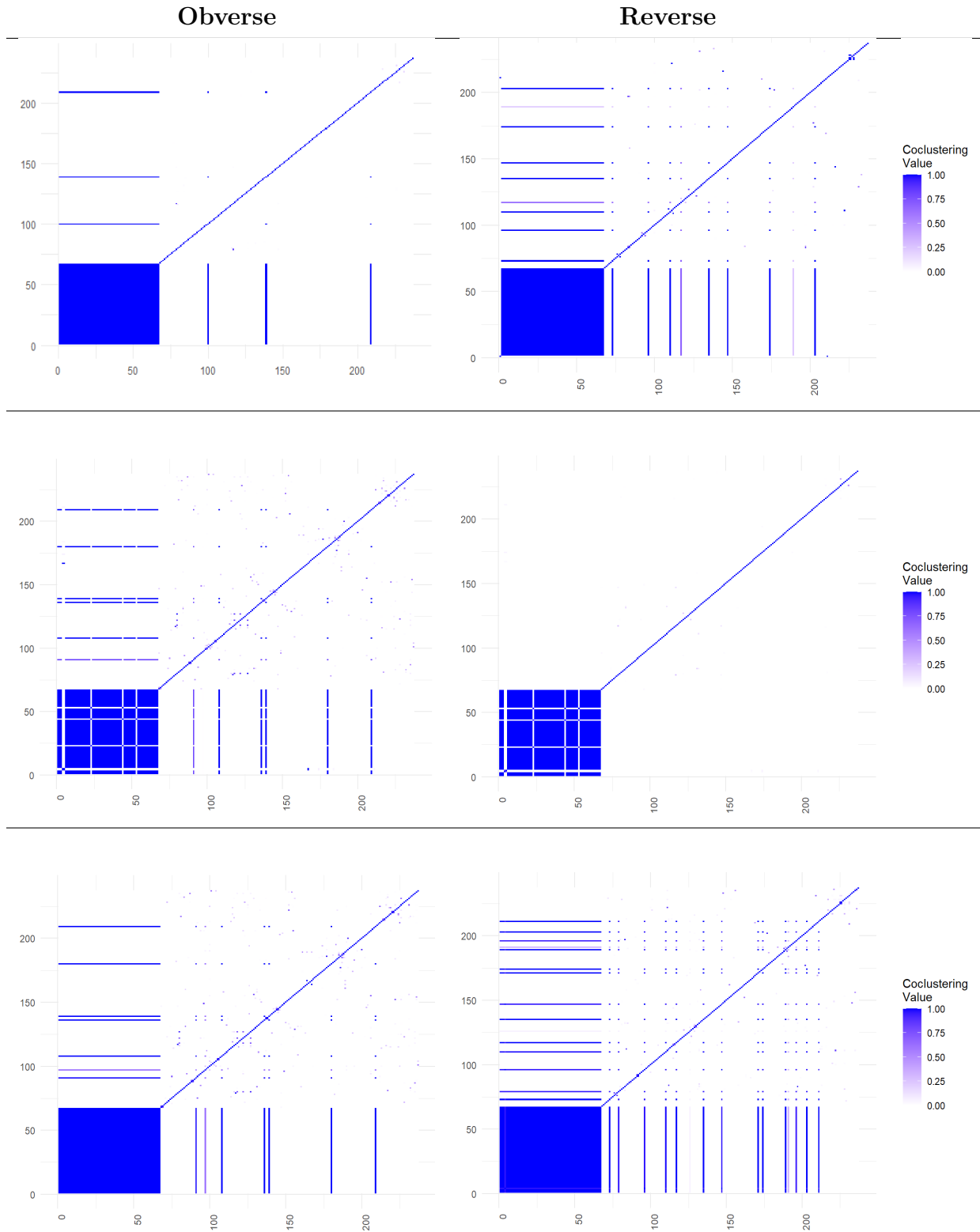


Table 7: Co-clustering matrices for the obverses and reverses for the joint Pitman-Yor model (first row), nested tessellation model (second row), and joint tessellation model (third row).